ELECTROSPINNING OF SILICA SUB-MICROTUBES MATS WITH PLATINUM NANOPARTICLES FOR NO CATALYTIC REDUCTION

Ramiro Ruiz-Rosas [a], Juana M. Rosas [a], Ignacio G. Loscertales [b], José Rodríguez-Mirasol [a,]*, Tomás Cordero [a].

[a] Chemical Engineering Department, School of Industrial Engineering, University of Málaga, c/ Doctor Ortiz Ramos s/n, Campus de Teatinos, 29071 Málaga, Spain.

[b] Department of Mechanical Engineering and Fluids Mechanic, School of Industrial Engineering, University of Málaga, c/ Doctor Ortiz Ramos s/n, Campus de Teatinos 29071 Málaga, Spain

* Corresponding author: Tel./Fax: (34) 951 952 385. e-mail: mirasol@uma.es

Abstract

Silica sub-microtubes loaded with platinum nanoparticles have been prepared in flexible non-woven mats using co-axial electrosppining technique. A partially gelated sol made from tetraethyl orthosilicate was used as the silica precursor, and oil was used as the sacrificial template for the hollow channel generation. Platinum has been supported on the wall of the tubes just adding the metallic precursor to the sol-gel, thus obtaining the supported catalyst by one-pot method. The silica tubes have a high aspect ratio with external/internal diameters of 400/200 nm and well-dispersed platinum nanoparticles of around 2 nm. This catalyst showed a high NO conversion with very high selectivity to N_2 at mild conditions in the presence of excess oxygen when using C_3H_6 as reducing agent. This relevant result reveals the potential of this technique to produce nanostructured catalysts onto easy to handle conformations.

Keywords: coaxial electrospinning, silica nanotubes, platinum nanoparticles, NOx SCR.

Graphical Abstract

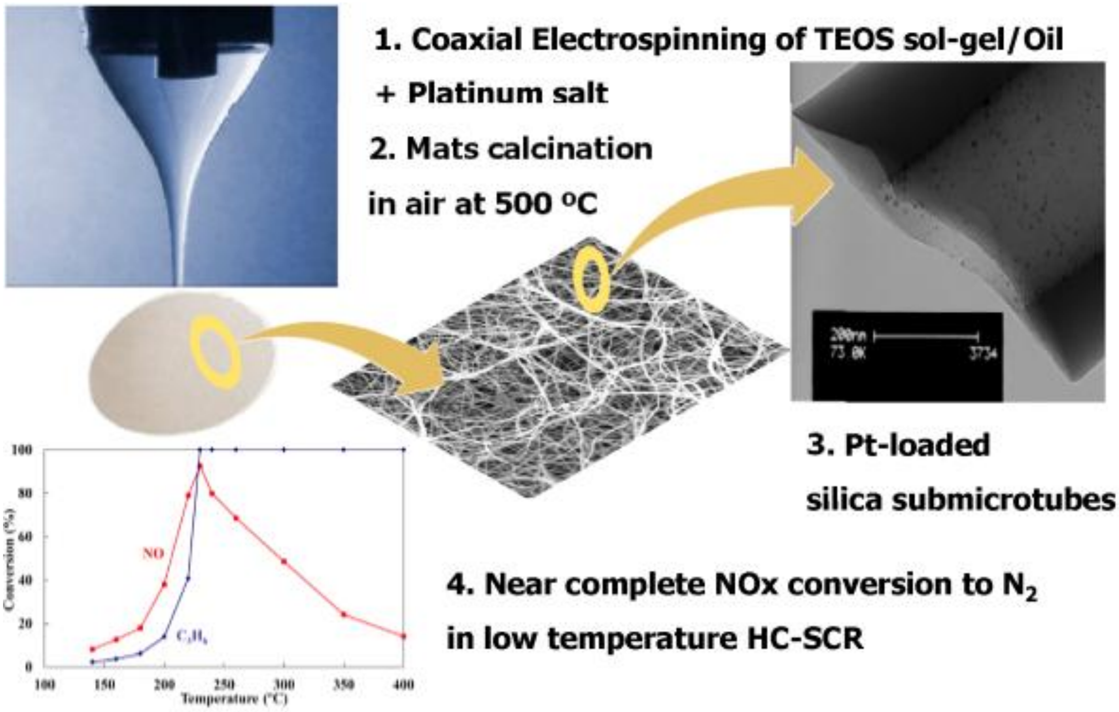

Highlights

- Non-woven mats of platinum-loaded silica nanotubes were obtained by co-axial electrospinning in one-pot procedure.
- By this technique, high dispersed Pt nanoparticles can be easily deposited on the walls of the silica nanotubes.
- Pt-loaded silica nanotube non-woven mats show high activity for low temperature NOx SCR with propylene in the presence of excess oxygen and outstanding N_2 selectivity, at the studied operation conditions.

1. INTRODUCTION

One dimensional nano- and sub-microstructured materials, such as fibers, wires or tubes show novel and interesting physical and chemical properties, which make them promising materials for applications in semiconductor, energy storage, sensor, optics or catalysis and play an important role in fundamental research [1-4]. In catalytic processes, pore diffusion resistance is significant in pellet shaped catalysts, while powdered catalysts, as is the practice in most laboratory-scale studies, are very hard to handle and could cause problems of high pressure drop in industrial size reactors. Therefore, novel forms of catalyst supports, as sub-microtubes catalysts, which are easy to handle, can be packed or constructed in the best form to fit the particular use and show very low resistance to diffusion [5], represent a key research issue for many catalytic industrial processes.

In this sense, electrospinning is a simple technique that has been used to obtain polymer and carbon fibers and tubes in the submicro- and nanoscale [6-11], in which a solution held in a capillary tube by its surface tension is subjected to an electric field that stretches the electrified jet due to the electrostatic repulsions between the surface charges and the evaporation of the solvent. The action of the electric field over a drop, forming at the tip of a capillary, changes its shape into a charged conical meniscus known as the Taylor cone [9]. Parameters such as viscosity and concentration of electrospun solution, flow rate and applied voltage control the diameter and length of fibers/tubes.

Moreover, using a co-axial electrospinning setup makes possible to switch from steady electrospray (droplets) to electrospinning (fibers/tubes) just controlling flow rate between outer and inner solutions. It also allows encapsulating of core liquid and the production of tubes [12,13]. The sol-gel technique has been widely studied for the preparation of different forms including monoliths, powders, coatings, and fibers [14,15]. In the case of silica forms, the typical sol-gel method consist of the hydrolysis and condensation of tetraethyl orthosilicate (TEOS), $Si(OCH_2CH_3)_4$.

In order to turn spinnable a solution is rather common to add some additives in the formulation, i.e. salts to improve conductivity or polymers to modulate the viscosity. This approach can also be profited to easily deposit metal catalysts on fiber/tubes just adding the metal precursor to the solution [11]. The presence of metal nanoparticles on the electrospun fiber/tube displays a huge potential in the area of heterogeneous catalysis. The diffusional constraints that can be found on most widely used catalyst conformation, i.e. spheres, pellets or layers over the wall of monoliths, may be reduced if the active phase is supported over the external walls of electrospun submicrosized fibers. Moreover, fibers could be directly casted as thin films over a support, or in form of flexible non-woven fabrics, which can be easily handled and deployed in any catalytic system.

Selective catalytic reduction (SCR) of NO to N_2 is a well-established technique readily available for the control of NOx emissions in stationary sources. SCR of NOx with hydrocarbons (HC-SCR) at low temperature ($T < 300$ ºC) under strongly oxidizing conditions is still a challenge and extensively studies have been carried out in the last years [16-18]. This technology seems to be especially suited for the case of emission control in diesel where more complete fuel combustion at excess oxygen and lower temperatures takes place, improving fuel economy. Platinum seems to be the most active metal for this case [19]. However, the main drawbacks of these Pt-based catalytic systems are the high selectivity to N_2O at low reaction temperatures and a narrow window of temperatures where high enough NOx conversion is achieved. The platinum particle size, oxidation state and the interaction with the support play an important role in the NOx reduction mechanism through the hydrocarbon activation over the catalyst surface [19-21]. More specifically, platinum supported on silica catalysts are reported to have a medium to high activity for NOx propylene-SCR, also showing higher chemical stability than alumina-supported catalysts when water or sulfur dioxide is present in the gas stream [22,23]. Nevertheless, activity and N_2 selectivity on NOx HC-SCR at low temperature for Pt-SiO_2 catalytic system are still to be enhanced.

In this work, we present the preparation and characterization of silica sub-microtubes with and without platinum nanoparticles using a sol-gel method followed by a coaxial-electrospinning process. One-dimensional structured materials with well dispersed platinum nanoparticles were obtained by a simple and straightforward one-pot process. Silica sub-microtubes with 1% platinum were used as catalysts for NO reduction with propylene in the presence of oxygen.

2. MATERIALS AND METHODS

2.1 Catalyst preparation

The silica sol was prepared from TEOS, ethanol, distilled water, and HCl. The sol composition in molar ratio was 1:2:2:0.025 (TEOS:ethanol:water:HCl). First, the HCl was mixed with water. Once diluted, ethanol was added to the solution. This solution is added to the TEOS. The acid catalyzes the hydrolysis reaction, which is strongly exothermic, and the TEOS is dissolved. The mixture, stirred vigorously, was heated up to 80 ºC for 1 h and then cooled down to 60 ºC. In the case of the tubes containing platinum, platinum (II) acetylacetonate was added to the solution at 60 ºC in a molar ratio to TEOS of 0.006. The solutions (with and without platinum) were maintained at this temperature under stirring for approximately 48 h in order to evaporate the alcohols formed during the condensation phase of the sol gel and to reach the viscosity required for turning the gel spinnable by this technique. By this way, the solidification of the partially gelated TEOS during the fly of the jet to the collector is ensured, thus avoiding the breaking up of the jet because the prevalence of a varicose instability. Silica sub-microtubes were generated by using the coaxial electrospinning method reported in the literature [12] in a co-axial configuration, with the sol gel, which plays the role of carrier, coming through the external capillary tip and synthetic oil flowing through the inner one (Figure 1). Both liquid viscosities were high enough to allow the viscous forces to overcome the liquid-liquid surface tension so the TEOS gel can drag the oil template, forming a compound Taylor cone [12]. The synthetic oil will act as a template fluid producing the tube conformation after its removal. The flow rates through the needles were around 0.6/1.5 $mL \cdot h^{-1}$ for sol gel/synthetic oil, respectively. To apply the high voltage between the spinneret and the collector (Figure 1), two high voltage power supplies are used: one positively polarized connected to the needle and the other negatively polarized attached to a collector. This configuration provided better electrostatic conditions to prevent tubes from flying to any grounded piece near the set-up, therefore facilitating the deposition of the electrospun tubes on the collector. The tip-to-collector distance was 20–25 cm, and the electrical potential difference was 10 kV (the collector was at –5 kV and the tips at +5 kV), although this value could slightly varied depending on the collector/tip geometry.

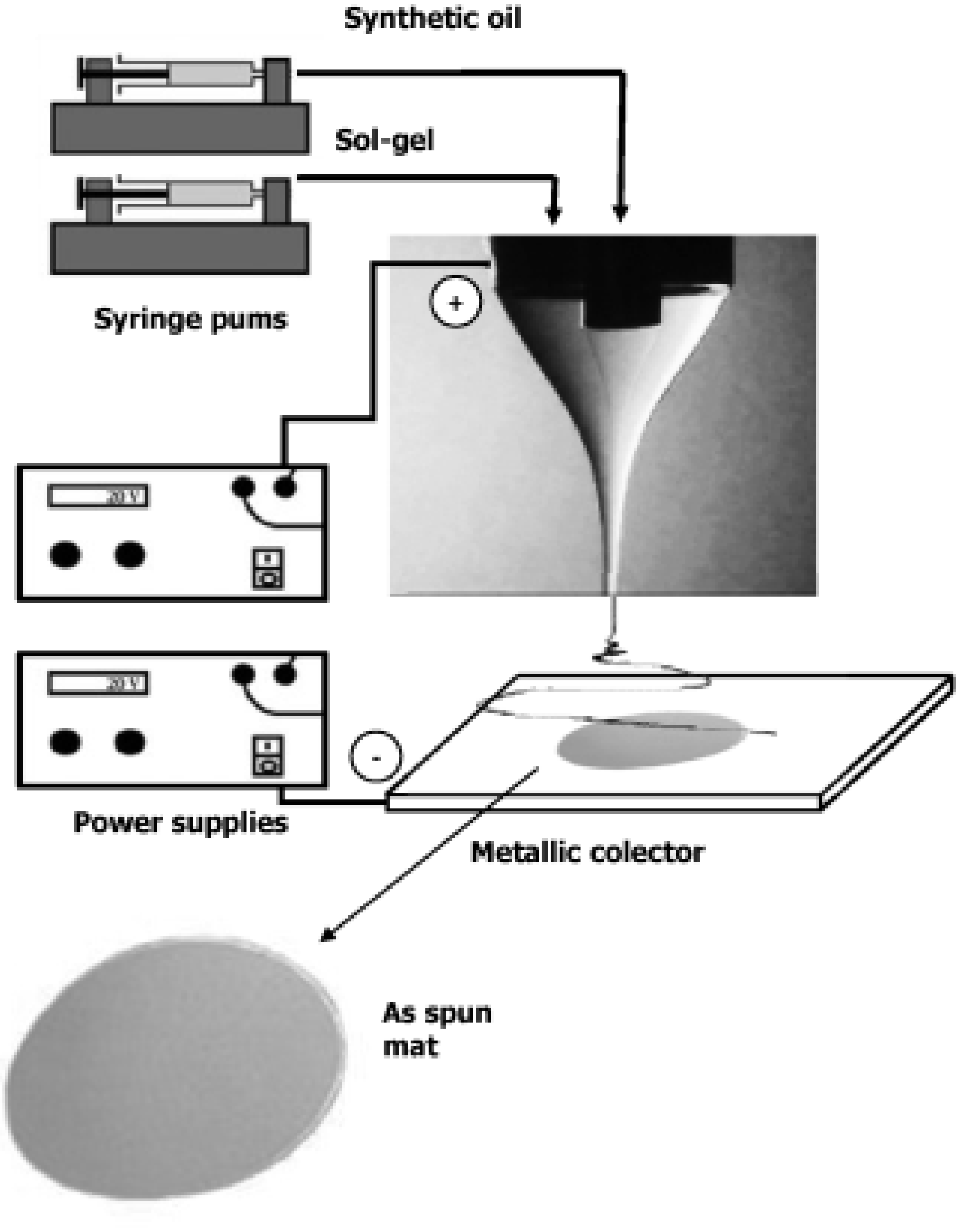

Figure 1. Coaxial electrospinning set up for the preparation of the catalysts

The electrospun tubes with and without platinum were easily collected as a flexible non-woven mat, Fig. 1, and are referred as SiT-Pt and SiT, respectively. Finally, the electrospun tubes were calcined at 500 ºC for 2 hours in a muffle furnace, in order to eliminate the solvents and the synthetic oil and stabilize the silica tubes. Silica nanotubes with and without platinum are denoted as SSiT-Pt and SSiT, respectively. The stabilized (calcined) electrospun mats acquired a cotton-like texture, and although they turned more brittle under mechanical pressure, they kept enough mechanical stiffness and flexibility to allow their easy manipulation without compromising the membrane structural integrity.

2.2 Catalyst characterization

Thermogravimetric analysis (TG) were performed in a CI Electronics MK2 balance under air flow (150 cm^3 STP/min) from room temperature to 900 ºC at a heating rate of 10 ºC/min with a sample weight of about 10 mg. X-ray diffraction patterns (XRD) were recorded in the region of $2\theta = 5\text{-}80º$ on a Philips X’Pert PRO MPD diffractometer using CuKα monochromatic radiation (operation value 45 kV and 40 mA).

The porous structure was characterized by N_2 adsorption-desorption at -196 ºC and by CO_2 adsorption at 0 ºC, carried out in a Micromeritics ASAP2020 apparatus. Samples were previously outgassed for 8 hours at 150 ºC under vacuum. From the N_2 adsorption/desorption isotherm, the apparent surface area (A_{BET}) was calculated by applying the BET equation. Micropore volume (V_{DR}) was estimated by applying the Dubinin-Raduskevich equation on the low pressure adsorption branch [24], while the application of t method using Harkins and Jura equation allows the estimation of external surface area (A_t). CO_2 adsorption isotherm at 0 ºC was used to assess the narrow micropore surface area, $A_{DR(CO2)}$, and micropore volume, $V_{DR(CO2)}$. The surface chemistry of the samples was studied by X-ray photoelectron spectroscopy (XPS) analysis, using a 5700C model Physical Electronics apparatus with MgKα radiation (1253.6 eV). For the analysis of the XPS peaks, the C1s peak position was set at 284.5 eV and used as reference to locate the other peaks. The fitting of the XPS peaks was done by least squares using Gaussian-Lorentzian peak shapes. Fourier transform infrared (FTIR) spectra were obtained using a Bruker Optics Tensor 27 FT-IR spectrometer by adding 256 scans in the 4000-400 cm^{-1} spectral range at 4 cm^{-1} resolution. Pressed KBr pellets at a sample/KBr ratio of around 1:250 were used.

The surface and inner morphology of the tubes was studied by scanning electron microscopy (SEM) using a JSM 840 JEOL microscope working at 25 KV voltage and by transmission electron microscopy (TEM) in a Philips CM200 microscope at an accelerating voltage of 200 kV. Platinum size distribution of the SSiT-Pt sample was obtained by counting 150 particles approximately. The size distribution was fitted to a normal distribution. From the size distribution, we determined the number average diameter [25]. Platinum particle size (assuming spherical particles) and dispersion (D) are related by D = 108/dn (nm) [26].

2.3 NO Selective Catalytic Reduction (SCR) experiments

The NO reduction experiments were performed in a quartz fixed bed microreactor (4 mm i.d.) at atmospheric pressure. Experiments were carried out with 80 mg of stabilized tubes (SSiT or SSiT-Pt). The inlet flow rate used was 200 cm^3 STP/min, with NO concentration of 400 ppm, resulting in a space time of W/FNO = 1.44 g·s/µmol. The concentrations of other inlet gases were 3% for O_2, 1500 ppm for C_3H_6 and 1000 ppm for CO. A chemiluminiscent analyzer (EcoPhysics, CLD 700 AL model) was used to measure the outlet gas concentrations of NO and NO_2. The CO and CO_2 outlet concentrations were analyzed by means of a non-dispersive infra-red analyser (Ultramat 22, Siemens model). C_3H_6, H_2O, N_2, N_2O and O_2 concentrations were measured by a mass spectrometer analyzer (Balzers MsCube).

3. RESULTS AND DISCUSSION

3.1 Air calcination of as-spun mats

TGA experiments were conducted over the as-spun tubes for selecting a desirable air calcination temperature. Figure 2 represents the weight loss of the silica tubes with and without platinum and of the synthetic oil used as template in the electrospinning process as a function of temperature, from room temperature to 900 ºC, at a heating rate of 10 ºC/min in air atmosphere. TGA results revealed different steps in the degradation of the template oil under oxygen atmosphere, probably corresponding to decomposition of unsaturated and saturated fatty acids which are the main component of oils [27] and also the oxidation of carbon residue. In the case of the tubes, the mass loss begins at temperatures lower than 100 ºC due to the evaporation of the solvents used in the formulation of the silica tubes. The TGA profiles for the tubes show a significant mass loss, beginning at around 300 ºC and finishing at about 500-600 ºC, matching those observed for the synthetic oil used as template and, therefore, associated to the decomposition and oxidation of the oil remaining in the inner of the non stablized silica tubes. This mass loss is more pronounced and starts at lower temperature for the SiT-Pt tubes than for the SiT ones, probably as a consequence of the catalytic effect of the platinum in the decomposition and oxidation reaction. The slow weight loss observed for the tubes with increasing temperature up to around 700 ºC is probably due to the water molecules released during the self-condensation reaction of the silanol groups [28]. Thus, 500ºC was set as the final temperature for air calcination of the silica tubes with and without Pt.

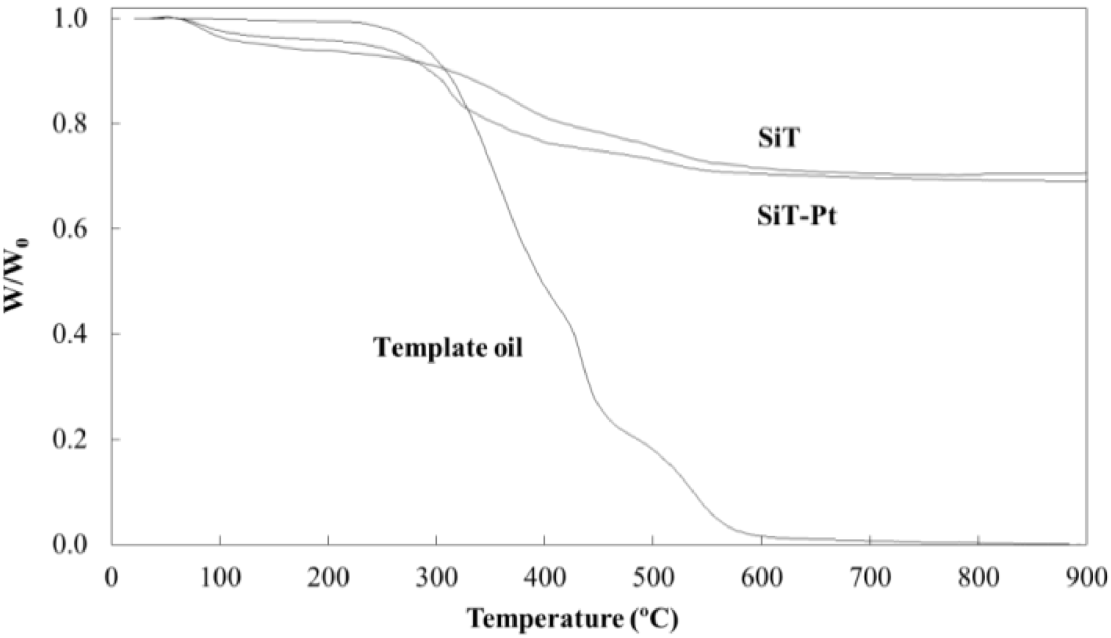

Figure 2. TG profiles in air atmosphere of the as-spun sub-microtubes with and without platinum and the synthetic oil used as template in the electrospinning process

3.2 Nanotubes morphology

The morphology of the prepared mats was analyzed by SEM. Figures 3 a to d show selected micrographs of the SiT, SSiT and SSiT-Pt samples. It can be seen that these mats consist in a non-woven fabric of submicrometric hollow fibers. The size and shape of these hollow fibers were very uniform in the as-spun mat, and no sintering or beads were found (Fig. 3a). Furthermore, the hollow fibers show a high aspect ratio (ratio between the length and the diameter of the fiber), with diameters clearly lower than 1 µm. Neither the calcination process nor the introduction of platinum show a significant influence on the morphology or size of the resulting fibers, Fig 3b-c. Figure

3.d provides evidence of the hollow channel induced by the template removal in these forms, which can be seen at the tip of some broken tubes.

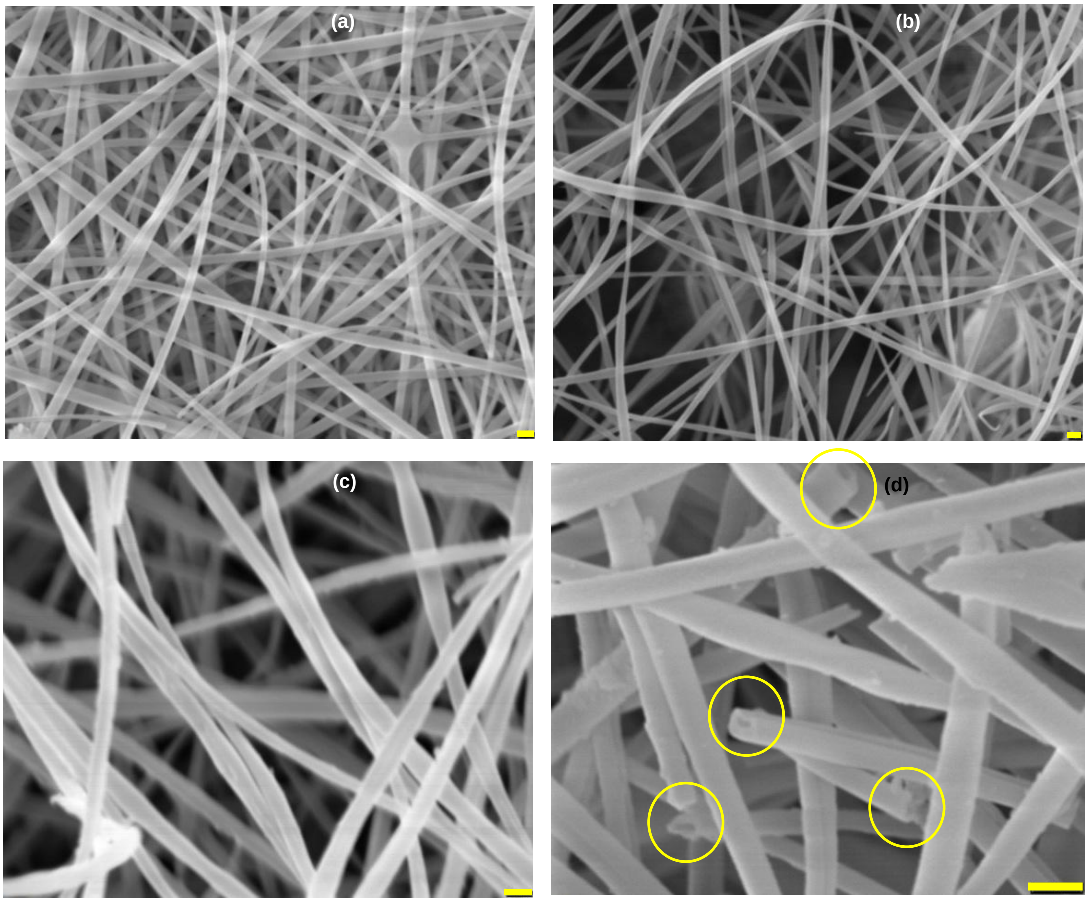

Figure 3. SEM images of (a) SiT, (b) SSiT, (c) and (d) SSiT-Pt (bars length: 1 µm)

Co-axial electrospinning is a powerful technique to prepare hollow fibers of controlled sizes. The wall width can be adjusted by fine-tuning the delivery rate of the template and gel to the Taylor cone. Varying the template/gel flow ratio between 1/1 and 3.5/1 while keeping the carrier rate at 0.6 $mL{\cdot}h^{-1}$ caused an increase in both the size of the channel inside the silica fiber and the external diameter. When oil was fed at rates lower than 0.8 $mL{\cdot}h^{-1}$, the occurrence of inner dripping mode started to happen (i.e., the outer liquid encapsulates the inner one in small droplets). On the other hand, delivery rates over 1.6 $mL{\cdot}h^{-1}$ further reduced the silica wall thickness to values lower than 100 nm, but caused the appearance of shape and size irregularities. The delivery rates were set to 0.6 and 1.6 mL·h^{-1} for the TEOS and oil template solutions, respectively, seeking to ensure a continuous fibril hollow shape. Fig. 4a displays TEM images of uniform and smooth nanotubes of SiT, with high aspect ratio. They lack structural defects and show external diameters of approximately 400 nm and internal diameter sizes of around 200 nm. Figure 4b represents a higher magnification TEM image of a silica tube obtained after air calcination. This tube shows likewise an external diameter of 346 nm and a hollow size of 122 nm, proving that calcination did not substantially modify the morphology of the tubes. The selected-area electron diffraction pattern (SAED) of the stabilized tubes (detail in Figure 4b) shows no diffraction patterns, pointing out the amorphous structure of the silica tubes.

The huge flexibility and control that electrospinning brings over the decoration of platinum nanoparticles is reflected in the TEM images on Figure 4c-d. In the formulation of the mat showed in this image, a platinic salt was added in the TEOS gel. Consequently, after the removal of the oil template during the calcination process, silica tube decorated with platinum nanoparticles were obtained. The addition of the platinum salt in the sol-gel precursor did not affect substantially the morphology of the nanotubes. Platinum nanoparticles were preferentially found on the internal wall of the tubes, Figure 4c, and also over the surface of the external wall of the tubes, Figure 4d. Detail on Figure 4c shows a higher magnification TEM image of a part of the surface of the stabilized tube with platinum. As can be seen, the tubes present platinum particles, showed as darker spots, which seem to be well-dispersed and essentially spherical, with sizes between 0.5 and 4 nm. Figure 5 shows the platinum particle size distribution histogram. It has been fitted to a normal distribution with mean μ and standard deviation σ. Based on this measurement, the average diameter size was 1.8 nm and the dispersion of the platinum is as high as 59.3%.

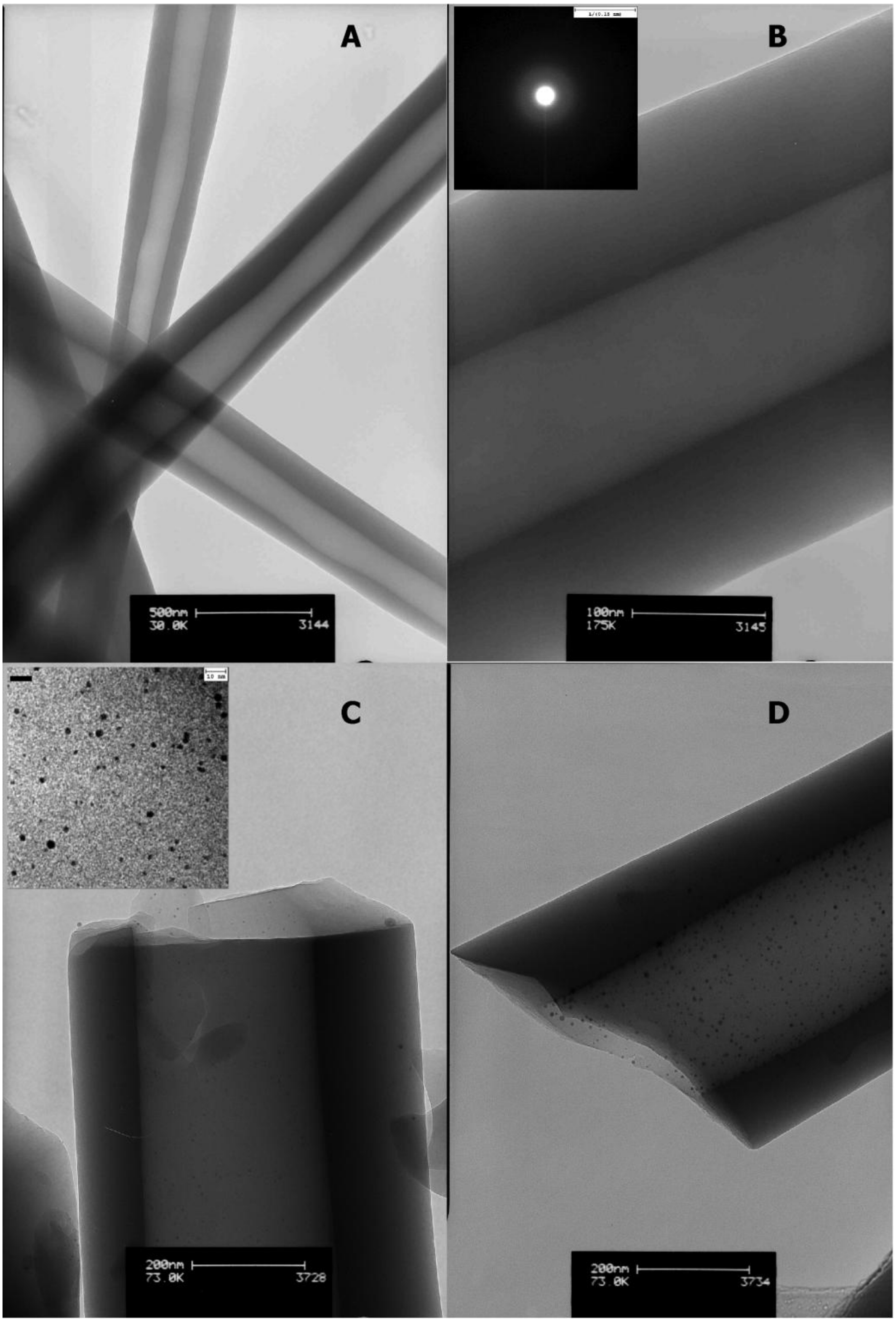

Figure 4. TEM images of (a) SSiT (bar length: 500 nm), (b) SSiT (bar length:100 nm), (c) SSiT-Pt (bar length: 200 nm) and (d) SSiT-Pt (bar length: 200 nm)

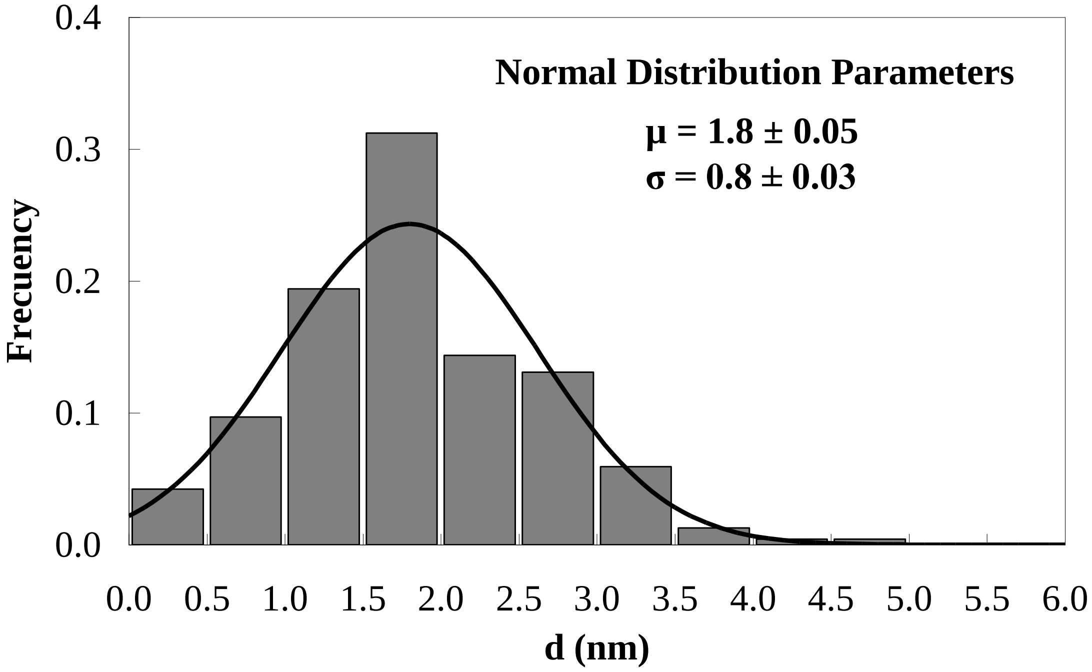

Figure 5. Platinum particle size distribution histogram of the SSiT-Pt sample

The benefits of using hollow fibers instead of solid ones when bringing accessibility to the active phase of a catalyst system can be illustrated in terms of their respective thiele modulus. The ratio between Thiele modulus, φ, for hollow to solid fibers is described as follows:

$$\frac{\varphi_{hollow}}{\varphi_{solid}} = \frac{w_{hollow}/2}{Rf_{solid}} \cdot \frac{\sqrt{k \cdot C^{n-1}/D_e}}{\sqrt{k \cdot C^{n-1}/D_e}} = \frac{w_{hollow}}{Rf_{solid}}$$

Where k, C^{n-1} and $D_e$stands for the kinetic rate, the bulk concentration of the reactive and the effective diffusivity, respectively. On the other hand, Rf_{solid} is the solid fiber radius, while w_{hollow} is the wall thickness of the hollow fiber, which is divided by 2 since the wall is accessible from both sides, thus reducing by half the molecular pathway inside it. Since in both solid and hollow fibers porosity, pore size distribution and connectivity are the same and the catalyst is evenly distributed, those parameters are to be equal for both conformations. Therefore the tube to fiber Thiele modulus ratio is

50/200 = 0.25. The generation of the hollow channel inside the fiber results in an important improvement on availability of the catalyst. As an outcome it can be claimed that the hollow fiber with external/internal diameters of 400/200 nm should face the same diffusional constraints than a 100 nm solid one.

3.3 Catalyst characterization

The crystalline structure of the silica tubes was studied by X-ray diffraction analysis. Figure 6 represents the XRD patterns of the pristine and air-calcined tubes with and without platinum, which exhibit the characteristics of amorphous silica [29]. In the case of the platinum containing samples, the peaks associated to the platinum crystal planes are not observed, probably as a consequence of well dispersed platinum in nanosized crystals.

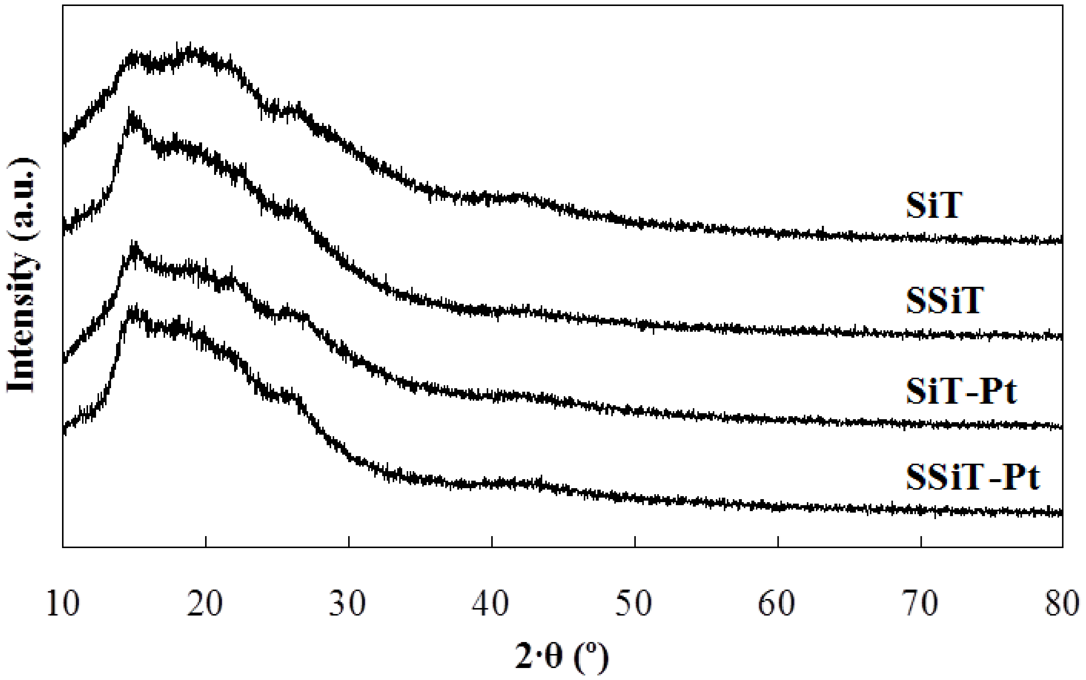

Figure 6. XRD patterns for as-spun and calcined samples

Figure 7 represents the FTIR spectrum of the non-stabilized and stabilized tubes with and without platinum. Broad transmission bands between 4000 and 3000 cm^{-1} are observed which correspond to the fundamental stretching vibrations of different types of hydroxyl groups [30]. The spectra clearly show two bands at 795 and 950 cm^{-1} associated to Si-O vibration in silanol groups (Si-OH). The bands at 1082 cm^{-1} are related to Si-O-Si groups. These groups are formed due to the hydrolysis and condensation of TEOS. After the calcination step, a decrease in the Si-OH band and an increase in the Si-O-Si band are obtained due to the complete condensation of hydrolyzed silica precursor (Si-OH) to silica (SiO_2) [31]. The band at 1625 cm^{-1} could be related to the combination of the SiO_2 vibrational modes. It should be noted the low intensity of the bands related to methyl (CH_3) or methylene (CH_2) located at around 2800-3000 and 1400-1800 cm^{-1}, respectively, on the as-spun fibers, related to a low contribution of methyl or methylene of ethoxy groups ($-OCH_2CH_3$), suggests that most of the TEOS is hydrolyzed. These bands mostly disappear in the spectra of the stabilized fiber, probably due to the decomposition and oxidation of the organic compounds (solvents and template oil) of the tubes during the calcination process.

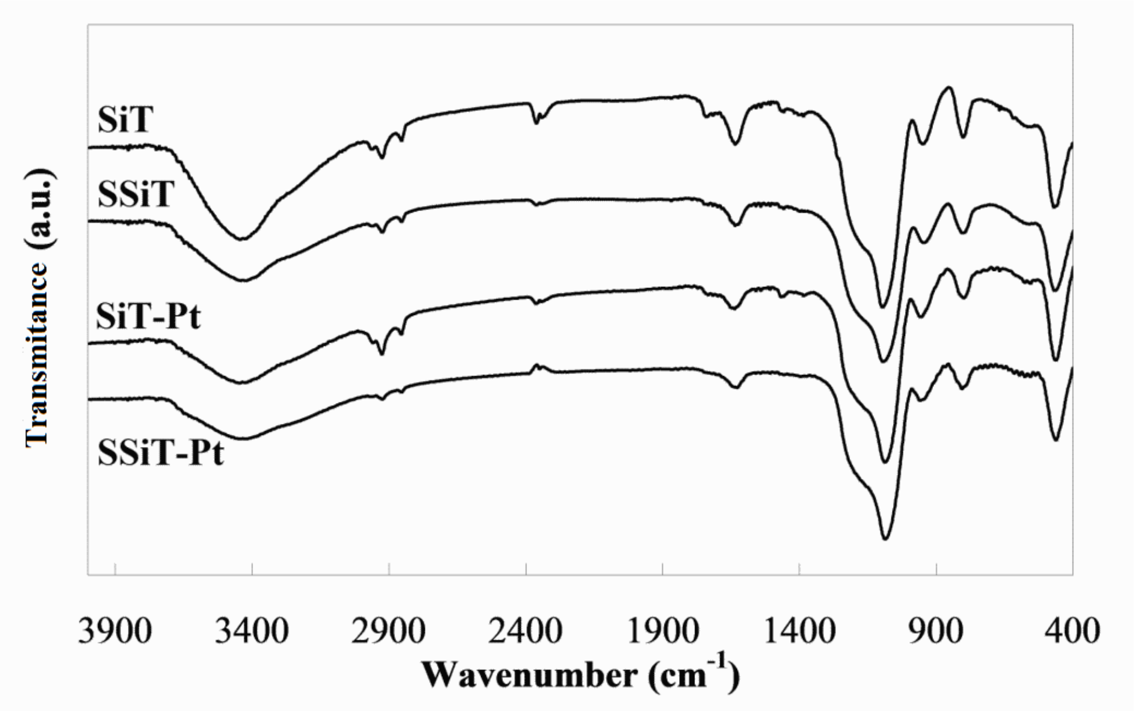

Figure 7. FTIR spectra of as-spun and calcined samples

The porous structure of the different tubes was analyzed by N_2 adsorption-desorption isotherms at -196 ºC and CO_2 adsorption at 0 ºC, and the results are shown in Table 1. The electrospun tubes with and without platinum, SiT-Pt and SiT respectively, show very low BET areas, as in non-porous solids. The similar values obtained for external surface area, A_t, and apparent surface area, A_{BET}, is manifesting that nitrogen is adsorbing mainly in the geometrical exposed area of the tube. The comparison of the apparent surface area obtained from the N_2 and CO_2 adsorption isotherms, with $A_{DR(CO2)} >> A_{BET}$, points out the presence of microporosity in these tubes, with mean pore size values under 0.7 nm [32]. The calcination process of SiT seems to produce the shrinkage of this narrow microporous structure. However, the presence of the platinum precursor results in a development of wide microporosity, measured with N_2 adsorption, resulting in silica tubes with total BET surface area of 144 $m^2 \cdot g^{-1}$. Lin et al. [33] reported that the addition of low Pt salt concentrations to the electrospinning of polyacrylonitrile/platinum acetylacetonate solution could increase the fiber diameters, due to the formation of polymer–salt–solvent interactions, which changed the balance among the viscosity, surface tension, and conductivity of the synthesis solutions. Unfortunately, they did not analyze the influence of the Pt salt on the fibers porosity. However, the porosity increase of the silica tubes can be ascribed to the decomposition of the platinum salt, which could act as a porosity template. In this sense, Ji et al. reported the production of porous carbon nanofibers from electrospun polyacrylonitrile (PAN)/SiO_2 composite nanofibers. After using hydrofluoric acid as etching agent, SiO_2 nanoparticles and agglomerates are removed from the carbon matrix, releasing new porosity inside them [34].

Table 1. Porous structural parameters of different silica sub-microtubes with and without platinum obtained from N_2 and CO_2 isotherms

Sample	$A_{BET(N2)}$ (m^2/g)	$A_{t(N2)}$ (m^2/g)	$A_{DR(CO2)}$ (m^2/g)	$V_{DR(N2)}$ (cm^3/g)	$V_{DR(CO2)}$ (cm^3/g)
SiT	3	2	228	--	0.087
SSiT	7	4	135	0.001	0.051
SiT-Pt	3	2	121	--	0.046
SSiT-Pt	144	13	273	0.056	0.104

Figure 8a shows the C1s spectra for the as-spun and air-stabilized silica tubes. The presence of platinum does not modify significantly the C1s spectra. The deconvoluted spectrum of the as-spun fibers show three different peaks, (i) at 284.5 eV associated to C-C and C-H bonds [35], (ii) at around 286.1 eV that could be related to C-OH groups [35] present in the ethanol used in the precursor solution and produced by the hydrolysis reaction of TEOS and (iii) at approximately 288.7 eV associated to the C-Si-O groups [30] from residual TEOS after the tube formulation. The calcination process removes almost all the carbon groups due to the evaporation of remaining ethanol and to the oxidation of the ethoxy groups and the organic compounds present in the synthetic oil, used as template of the tube. Thus, the C1s spectra of the stabilized tubes presents a main peak located at 284.5 eV probably due to adventitious carbon. The deconvoluted Si 2p spectra of SiT and SSiT tubes are also represented in Figure 8b. The spectrum of the as-spun nanotubes show a shift to lower binding energies that can be related to the presence of carbon atoms bonded to silicon. The chemical shift in the Si2p photoelectron signal is mainly induced by the number of oxygen atoms bound to a Si atom. When introducing carbon atoms into SiO_2, some of the four oxygen atoms bonded to the silicon are replaced by carbon atoms and the Si2p spectra shifts to lower binding energy values [36,37]. Furthermore, a slight asymmetry of the spectrum of as-spun tubes is observed. According to Ingo el al. [38], it could be associated to the presence of Si-O-CH_2CH_3 bonds from the precursor solution and it disappears when the sol-gel materials are subjected to air thermal treatments at temperatures higher than 400°C. This supports the presence of residual TEOS on the as-spun SiT sample. After air stabilization, the organic matter has been removed and all the silicon is in form of SiO_2.

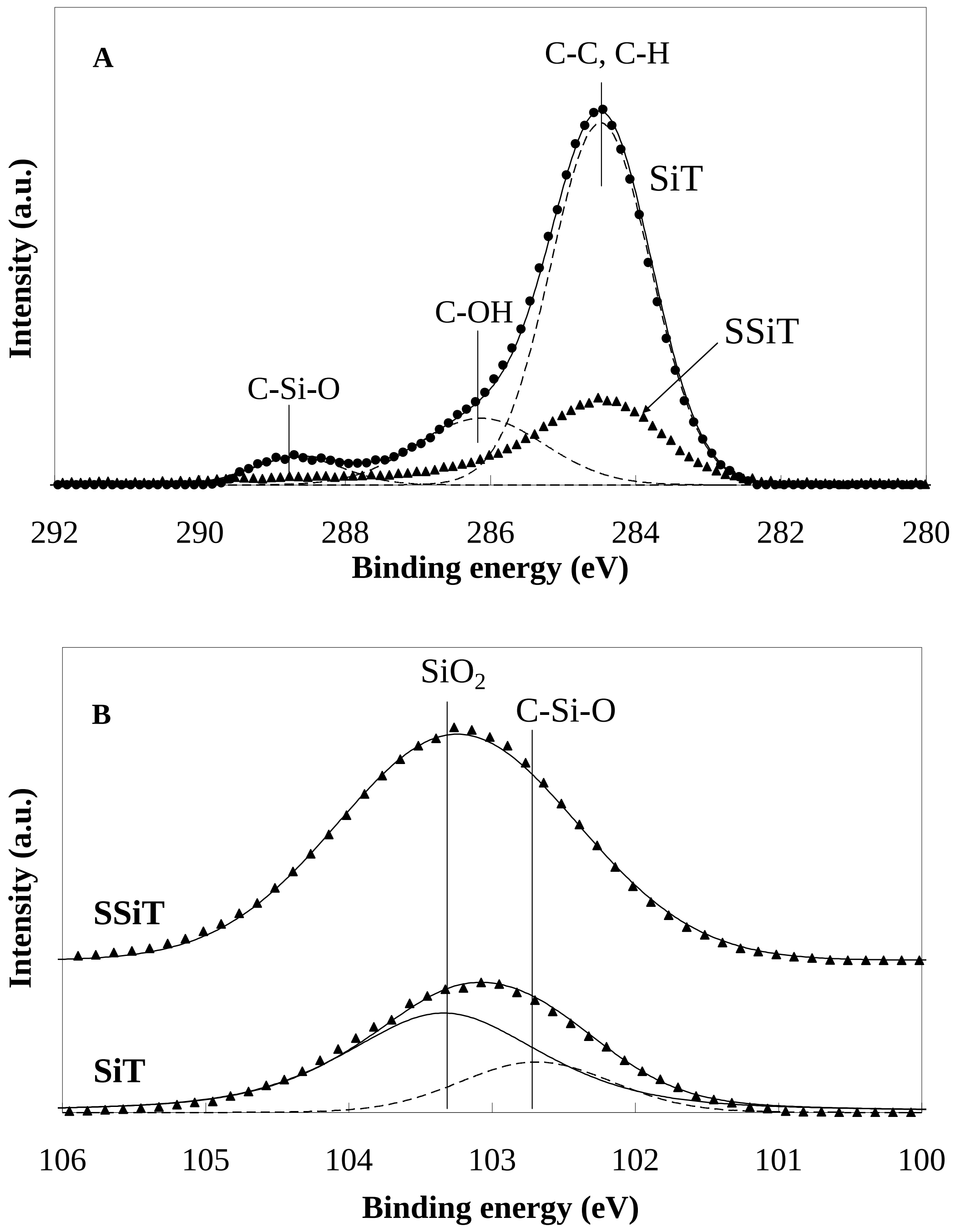

Figure 8. (a) XPS C 1s (a) and Si 2p (b) spectra of as spun and calcined silica tubes

Table 2 summarizes the atomic surface concentrations obtained from the numerical integration of the XPS peaks for the different silica tubes. The amount of surface silicon is much lower than that of carbon and oxygen for the non stalilized tubes. The stabilized (calcined) samples show much lower carbon content than that of the non-stabilized tubes, confirming the removal of organic compounds of the synthetic oil and the decomposition of remaining ethoxy groups and solvents on the sol-gel. The O/Si atomic ratio obtained after calcination is that corresponding to silica. In the case of the mats that contain platinum, the amount of surface platinum increases with the stabilization process, as a consequence of the removal of the organic part of the nanotubes. The platinum/silicon atomic ratio keeps constant at 0.004, which is lower than the value of 0.006 corresponding to the Pt/Si atomic ratio of the $Pt(AcAc)_2$/TEOS initial solution. The stabilized silica tubes with platinum show a platinum atomic surface concentration of 0.12%, which corresponds to a weight surface concentration of 1.20%, somehow lower than that of the theoretical value from the tubes formulation, 1.91%. This result and the relatively high surface area value obtained for the silica tubes with platinum, corresponding mainly to micropores, suggest that a relatively large amount of the platinum is probably on the internal surface of the tube (micropores), out of the penetration range of the XPS analysis. Moreover, the reduction observed for the $A_{DR(CO2)}$ value from 228 m^2/g for SiT to 121 m^2/g for SiT-Pt (Table 2) suggests that the Pt precursor is located in part of the micropores. After calcination of SiT-Pt, the value of $A_{DR(CO2)}$ increases to 273 m^2/g, as a consequence of Pt precursor decomposition, with a significant increase of the $A_{BET(N2)}$ to 144 m^2/g.

Table 2. Atomic surface concentration (%) of different silica sub-microtubes with and without platinum determined by XPS quantitative analysis.

Sample	%C	%O	%Si	%Pt
SiT	48.6	35.5	15.9	--
SSiT	11.0	60.5	28.5	--
SiT-Pt	57.7	31.7	10.6	0.0(4)
SSiT-Pt	9.8	60.1	30.0	0.1(2)

The oxidation state of platinum was studied by XPS. Figure 9 displays the Pt 4f spectra for the Pt containing non-stabilized and stabilized tubes. The Pt 4f region of these tubes presents a doublet corresponding to Pt $4f_{7/2}$ and Pt $4f_{5/2}$ [35]. The separation between Pt $4f_{7/2}$ and Pt $4f_{5/2}$ peaks, due to spin orbital splitting, is a quantized value of 3.33 eV. The Pt $4f_{7/2}$ peak lying at around 71.0 eV can be attributed to Pt^0 (metallic Pt), while the Pt $4f_{7/2}$ peak located at around 72.8 eV is related to Pt^{2+} (electrodeficient platinum) [35]. Platinum is mostly in form of Pt^{2+} on the non-stabilized tubes in agreement with the oxidation state of platinum in the precursor. The air stabilization process produces an increase and a shift of the peaks to lower binding energies, which indicate the presence of a higher contribution of platinum in form of Pt^0 on the surface of the stabilized tubes. Probably, during the air calcination process most of the organic compounds are oxidized, producing CO among other gases, which is a reducer gas. In this sense, Cavaliere et al. [39] reported the elaboration of Pt loaded titania nanofibres and they also observed the presence of metallic Pt. They associated these results to the alcohol present as traces of solvent, or formed during the hydrolysis of the TiO_2 precursor, which reduces the Pt^{2+} in the presence of PVP, leading directly to metallic Pt nanoclusters, without the need for a subsequent reduction step [40]. However, they did not exclude that C or CO produced during the thermal decomposition of ethanol and PVP participates in reduction of Pt^{2+}.

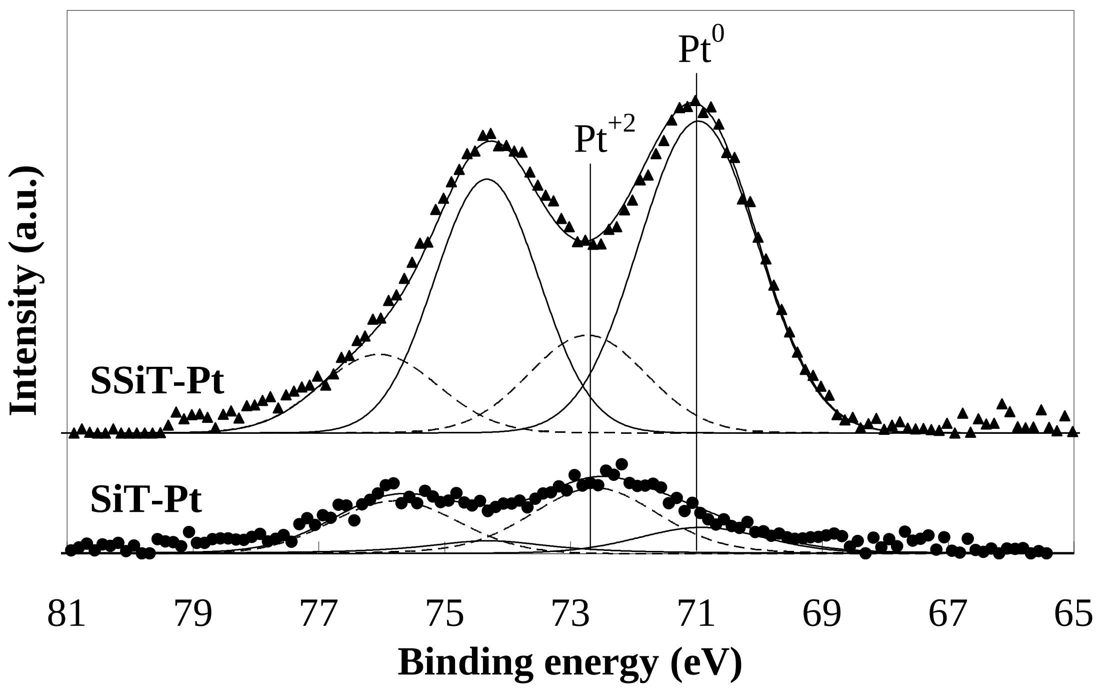

Figure 9. Deconvoluted XPS Pt 4f spectra of Pt-loaded samples

3.4. Catalytic NO conversion.

The catalytic oxidation of NO and the selective catalytic reduction (SCR) of NO with propylene in the presence of oxygen with and without SO_2 and CO was studied for the platinum-loaded stabilized tubes. The concentrations of these gases in the inlet stream of the reactor were set to be similar to those found in the exhaust of combustion engines. The catalysts in mat conformation were easily introduced in a fixed bed reactor just rolling the calcined membranes, slipping the rolled mat into the reactor and packing them with compressed air. SSiT, the silica submicrotube support without platinum, showed no catalytic effect for NO conversion. However, SSiT-Pt have shown a considerably NO conversion depending on the reaction conditions, proving that platinum is readily available for catalytic activity. The addition of C_3H_6 as reducing agent to the NO-containing gas flow fed to the fixed-bed reactor resulted in NO conversion even in excess of oxygen (3%), while no NO conversion was measured when CO was used as reductant agent.

Figure 10 shows NO and C_3H_6 conversion profiles as a function of temperature for the SSiT-Pt catalyst. A maximum NO conversion is observed at 225ºC, which lies inside the range of reported temperatures for this system, i.e., between 180 and 250 ºC. Propylene also reaches full conversion at the same temperature than that for NO maximum conversion. The volcano-shape of the NO profile is characteristic of these catalytic systems. This behavior has been interpreted in terms of the competitive adsorption between NO and oxygen over the platinum active sites. At temperatures under the maximum NO conversion, adsorbed NO occupies most of the active sites, and propylene oxidation proceeds through interaction with adsorbed NO. In this sense, the propylene combustion temperature has been delayed for 40ºC in the presence of NO (C_3H_6 conversion profile in absence of NO is not shown for clarity sake), supporting the predominant role of NO as the oxidizing agent at low temperatures. At temperatures higher than that of maximum NO conversion, O_2 adsorption is favored, being most of the active sites occupied by oxygen. Accordingly, the adsorbed oxygen drives the propylene oxidation at such temperatures [22].

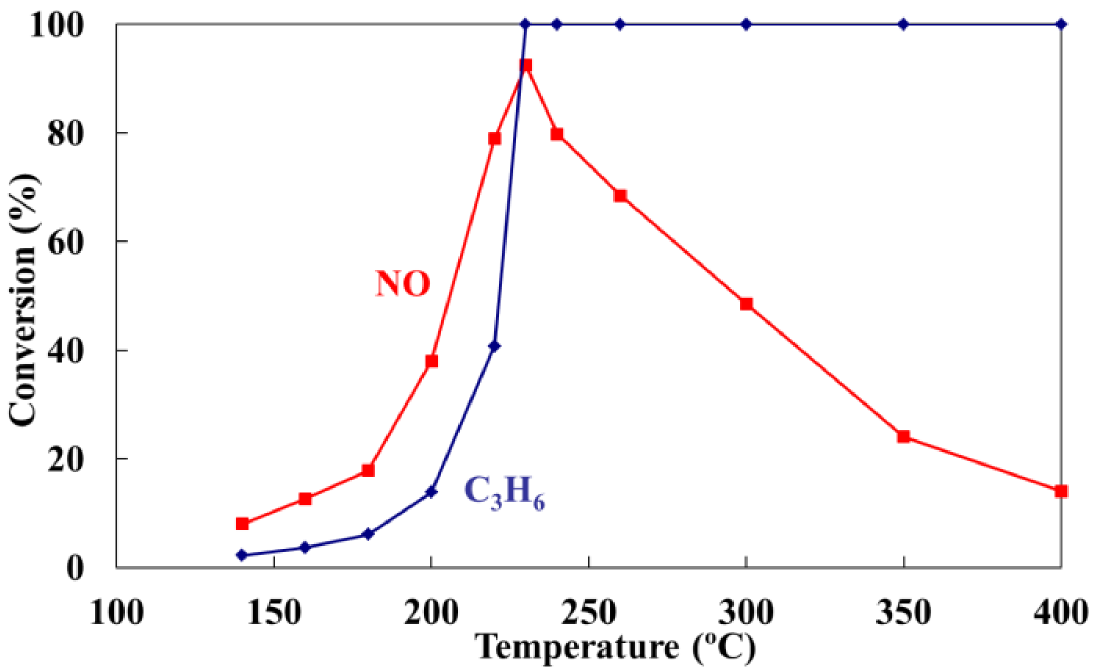

Figure 10. NO (400ppmv) and C_3H_6 (1500ppmv) conversion in the presence of oxygen (3%) as a function of reaction temperature, W/F_{NO}= 2.88 g·s/µmol.

NO conversion reached a steady-state value of about 90% at 225ºC, being higher than 80% between 210 and 240ºC. The temperature window where the catalyst can operate at full condition, i.e., high NO conversion, is slightly narrower than in other platinum based catalysts reported in the literature with a similar metal loading, which also showed comparable or slightly higher conversion values at analogous reaction conditions. Nevertheless, only NO, N_2, CO_2 and H_2O were detected in the outlet gas stream up to 350ºC, indicating that the reacted NO was reduced to N_2, while all the C_3H_6 was oxidized to CO_2 and H_2O. It is important to point out that one of the main drawbacks reported in the literature for platinum catalysts is the significant selectivity towards N_2O [17-22,39,41-45]. In the tested conditions, N_2O was not detected, so its steady-state concentration, if any, would be less than 5 ppmv. Same selectivity trend was observed when propylene concentration was reduced to 400 ppm.

Figure 11 represents the evolution of outlet gas concentration as a function of the reaction time using SSiT-Pt as catalyst for three experiments where the inlet gases were changed sequentially. For the first of them, Figure 11a, only NO diluted in He (200 ppm, W/F_{NO} = 2.88 g·s/µmol) was initially introduced in the reactor at 225ºC. After around 10 min, C_3H_6 (1500 ppm) was added to the inlet stream and, finally, at around 20 min of reaction time, O_2 (3% vol) was also introduced. In the first step only a low adsorption of NO was observed and no reaction products were detected. With the addition of propylene to the inlet stream, NO was partially desorbed, probably due to a competitive adsorption between NO and C_3H_6 molecules taking place on the active sites. With the addition of O_2, significant reduction of NO and the complete conversion of propylene were observed.

For the second experiment, SO_2 (1000 ppm) was added and later removed from an NO/O_2 gas stream (200 ppm NO, 3% O_2) (Fig 11b). In the first part of the experiment, partial NO oxidation to NO_2 is observed, which is linked to the well-known high activity of metallic platinum as oxidation catalyst. The addition of SO_2 to the inlet gas entirely inhibits the NO oxidation to NO_2 observed in the first step of the experiment. In this sense, Dawody et al. also reported a negative impact of SO_2 in NO oxidation by platinum in Pt/SiO_2 catalyst [46]. NO concentration in the outlet gas surpasses that of the inlet value when SO_2 was present, which could be related to unreacted NO molecules getting displaced from the adsorption sites by SO_2. This seems to be confirmed by the similar amount of NO desorbed in the second step (approx. 38 µmol/g) and the difference between removed NO and produced NO_2 in the first part of the experiment (~30 µmol/g). Furthermore, the adsorbed SO_2 amount (around 30 µmol/g) almost matches the displaced NO amount. As silica is known for showing low affinity for sulfur, the inhibition effect should be related to SO_2 adsorption over the platinum active sites. The nature of the interaction between SO_2 and platinum is reversible, as can be seen from the complete recovery of catalytic activity for NO oxidation when SO_2 was removed from the inlet gas after 120 minutes of reaction time.

The effect of the presence of SO_2 on NO C_3H_6-SCR conversion was also studied. Again, SO_2 (1000 ppm) was added to the inlet stream during the course of an NO C_3H_6-SCR experiment in the presence of oxygen (Figure 11c). After one hour, the initial gas stream composition was restored. NO conversion slightly decreased a 27.5% in the presence of SO_2 in the gas stream, while SO_2 outlet concentration soon reaches its inlet concentration. The propylene conversion and the selectivity towards N_2 formation remained constant. This result seems to point out that SO_2 competes with NO for adsorption over metallic platinum sites, whereas C_3H_6 adsorption could be favored over oxidized platinum sites (circa of 25% of total platinum amount, Figure 7). The inhibition of NO oxidation observed on Figure 11b along with the reduced impact on activity observed in this experience seems to point out that C_3H_6 oxidation reaction may also proceed through interaction between NO and the hydrocarbons adsorbed in a oxidized platinum site. Propylene adsorption would reduce the metal site, turning it active for NO adsorption and subsequent reduction. It is also interesting to observe that, after SO_2 has been removed from the feed stream, the catalyst activity for NO reduction is restored. Pt-loaded silica catalysts generally show high resistance to SO_2 poisoning for NO-SCR [44,46]. Neither sulfur species nor SO_2 evolution was detected by XPS or in the outlet gas during subsequent TPD after reaction, neglecting the possibility of SO_2 chemisorption or interaction with the adsorbed hydrocarbon.

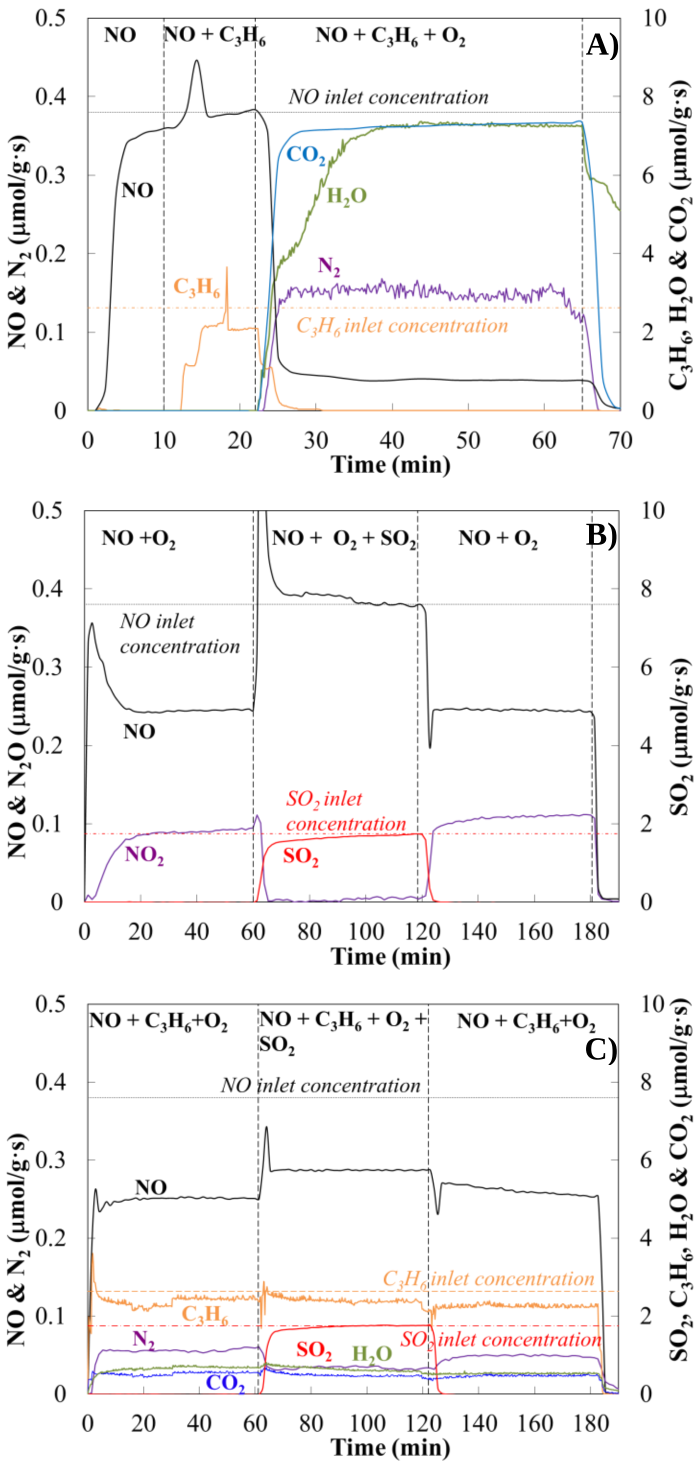

Figure 11. Evolution of outlet gas concentration as a function of reaction time for SSiT-Pt catalyst: a) using 200 ppm$_V$ NO, 3%v O_2 and 1500 ppm$_v$ C_3H_6, at 225 ºC; b) 200 ppm$_V$ NO, 3%v O_2 and 1000 ppm SO_2, at 200 ºC; c) 200 ppm$_V$ NO, 1500 ppm$_v$ C3H6, 3%v O_2 and 1000 ppm SO_2, at 200 ºC.

The technical literature proposes three main reaction pathways for low temperature selective catalytic reduction of NO on Pt catalysts. The first one involves production of molecular nitrogen through NO dissociative adsorption via a redox mechanism [47,48]. According to this scheme, NO is adsorbed on the Pt surface and dissociates to yield adsorbed nitrogen and oxygen atoms, which desorb in the form of molecular N_2 and N_2O. The role of the reductant is to react with adsorbed oxygen atoms and regenerate the active sites. Other authors propose that the activation of the hydrocarbon play the key role in the lean-DeNO$_x$ reaction. It occurs through reaction of the activated hydrocarbon with adsorbed NO or NO_2 [49-51] to form organo-nitro species that later decomposes as N_2 or N_2O. Finally, it has been also suggested that the adsorbed hydrocarbon can react with NO to form $C_xH_yO_zN_w$ species [52,53], which would be later removed from the surface by reaction with oxygen, thus regenerating the active sites.

In our case, although additional work is necessary to elucidate the most plausible reaction mechanism, it seems that the dissociative adsorption of NO can be disregarded, given that this is probably the main reaction pathway to produce N_2O. The NO dynamic adsorption experiments did not render noticeable N_2 or N_2O production, neither during adsorption itself nor during a subsequent temperature programmed desorption. Moreover, XPS analyses over SSiT-Pt sample after NO adsorption experiment did not detect any noticeable nitrogen presence (results not shown for brevity’s sake). A possible explanation for NO molecular adsorption being predominant over dissociate one would be the crystalline phase of platinum. The hexagonal crystalline phase, which has been related elsewhere to NO molecular adsorption [54], could be favored or stabilized by the silica support due to the particular catalyst preparation method used in this work.

There is some controversy regarding the role of NO_2 in NOx SCR. For instance, Pitchon et al. observed NO production at low temperatures for NO_2 HC-SCR with Pt-SiO_2 catalyst, which could be pointing out that NO_2 is previously reduced to NO before N_2 formation [52]. The oxidation of NO to NO_2 in the absence of a reductant agent could suggest that the formation of adsorbed NO_2, which would latter interact with the adsorbed hydrocarbon, could be likely to occur on this catalytic system, although the system response in the presence of SO_2, as shown in Figure 12.b and c, seems to neglect such a possibility. Therefore, the mechanism of NO reduction through reaction between an activated hydrocarbon and NO to form $C_xH_yO_zN_w$ species, which would later decomposed to N_2, CO_2 and water, should be considered as the most probable one.

4. CONCLUSIONS

One-dimensional microstructured catalysts with well dispersed metal nanoparticles have been obtained in form of submicronmeter silica tubes mats and used as catalysts in the NO reduction reaction in the presence of oxygen. The tubes have been obtained by co-axial electrospinning of a TEOS sol-gel and synthetic oil as template, using platinum (II) acetylacetonate as metal precursor, followed by a calcination process. The metal nanoparticles were casted into the wall of the tube just adding the platinum precursor in the TEOS gel. We have obtained silica tubes with external/internal diameters of around 400/200 nm, respectively, and with well dispersed platinum nanoparticles of about 1.8 nm in size. The silica nanotubes doped with platinum revealed some microporosity development and an amorphous crystalline structure. These mats were tested as catalysts for the selective NO reduction reaction. The platinum loaded nanotubes show a high NO conversion when using C_3H_6 as reducing agent in the presence of oxygen, comparing fairly well with other SiO_2-Pt catalysts reported in the literature. Outstanding selectivity to N_2 at mild temperature was achieved. The presence of SO_2 during NO C_3H_6-SCR partially hinders the NO conversion, probably due to competitive adsorption between SO_2 and NO. Nevertheless, the catalytic activity of the SSiT-Pt mat was restored after removal of SO_2 from the gas inlet. The absence of N_2O formation during the NO reduction by propylene in the presence of oxygen seems to point out to a mechanism related to lack of dissociative NO adsorption over Pt active sites.

ACKNOWLEDGMENTS

This work was supported by the Spanish Ministry of Science and Innovation under CTQ2009/14262 project and by Spanish Ministry of Economy and Competitiveness under CTQ2012-36408 project.

5. REFERENCES

1. C.M. Lieber, MRS Bull. 28 (2003) 486-491.

2. J. Xiang, W. Lu, Y.J. Hu, Y. Wu, H. Yan, C.M. Lieber, Nature 441 (2006) 489-493.

3. M. Law, J. Goldberger, P.D. Yang, Annu. Rev. Mater. Res. 34 (2004) 83-122.

4. Y.N. Xia, P.D. Yang, Y.G. Sun, Y.Y. Wu, B. Mayers, B. Gates, Y.D. Yin, F. Kim, Y.Q. Yan, Adv. Mater. 15 (2003) 353-389.

5. Y. Matatov-Meytal, V. Barelko, I. Yuranov, M. Sheintuch, Appl. Catal. B-Environ. 27 (2000) 127-135.

6. D.H. Reneker, I. Chun, Nanotechnology 7 (1996) 216-223.

7. Z.-M. Huang, Y.-Z. Zhang, M. Kotaki, S. Ramakrishna, Comp. Sci. Technol. 63 (2003) 2223-2253.

8. I.G. Loscertales, A. Barrero, M. Márquez, R. Spretz, R. Velarde-Ortiz, G. Larsen, J. Am. Chem. Soc. 126 (2004) 5376-5377.

9. G. Larsen, R. Velarde-Ortiz, K. Minchow, A. Barrero, I.G. Loscertales, J. Am. Chem. Soc. 125 (2003) 1154–1155.

10. M. Lallave, J. Bedia, R. Ruiz-Rosas, J. Rodríguez-Mirasol, T. Cordero, J.C. Otero, M. Marquez, A. Barrero, I.G. Loscertales Adv. Mater. 19 (2007) 4292-4296.

11. R. Ruiz-Rosas, J. Bedia, M. Lallave, I.G. Loscertales, A. Barrero, J. Rodríguez-Mirasol, T. Cordero, Carbon 48 (2010) 696-705.

12. I.G. Loscertales, A. Barrero, I. Guerrero, R. Cortijo, M. Márquez, A.M. Gañán-Calvo, Science 295 (2002) 1695-1698.

13. J.E. Díaz, A. Barrero, M. Marquez, I.G. Loscertales, Adv. Func. Mater. 2006, 16, 2110-2116.

14. R.D. Gonzalez, T. Lopez, R. Gomez, Catal. Today 35 (1997) 293-317.

15. R. Ruiz-Rosas, J. Bedia, J.M. Rosas, M. Lallave, I.G. Loscertales, J. Rodríguez-Mirasol, T. Cordero, Catal. Today 187 (2012) 77–87.

16. M. Khosravi, C. Sola, A. Abedi, R.E. Hayes, W.S. Epling, M. Votsmeier, Appl. Catal. B-Environ. 147 (2014) 264-274.

17. E. Santillan-Jimenez, V. Miljković-Kocić, M. Crocker, K. Wilson, Appl. Catal. B-Environ. 102 (2011) 1-8.

18. E. Santillan-Jimenez, Mark Crocker, A. Bueno-López, C. Salinas-Martínez de Lecea, Ind. Eng. Chem. Res. 50 (2011) 7191-7200.

19. R. Burch, P.J. Millington, Catal. Today. 26 (1995) 185-206.

20. J.M. García-Cortés, J. Pérez-Ramírez, J.N. Rouzeaud, A.R. Vaccaro, M.J. llán-Gómez, C. Salinas-Martínez de Lecea, J. Catal. 218 (2003) 111-122.

21. J.M. García-Cortés, J. Pérez-Ramírez, M.J. Illán-Gómez, F. Kapteijn, J.A. Moulijn, C. Salinas-Martínez de Lecea, Appl. Catal. B-Environ. 30 (2001) 399-408.

22. R. Burch, P.J. Millington, Catal. Today 29 (1996) 37-42.

23. R. Burch, T.C. Watling, Appl. Catal. B-Environ. 17 (1998) 131-139.

24. S.J. Gregg, K.S.W. Sing, Adsorption, surface area and porosity, 2nd edition, Academic Press, London, 1982.

25. M.A. Vannice, Kinetics of Catalytic Reactions. Springer, New York, USA, 2005, 20.

26. R.J. Farrauto, C.H. Bartholomew, Fundamentals of Industrial Catalytic Processes. Blackie Academic & Professional, NY, 1997.

27. J.C.O. Santos, I.M.G. Santos, M.M. Conceiçăo, S.L. Porto, M.F.S. Trindade, A.G. Souza, S. Prasad, V.J. Fernandes, A.S. Araújo, J. Therm. Anal. Calorim. 75 (2004) 419-428.

28. W.L. Huang, S.H. Cui, K.M. Liang, Z.F. Yuan, S.R. Gu, J. Phys. Chem. Solids 63 (2002) 645-650.

29. S.S. Choi, S.G. Lee, S.S. Im, S.H. Kim, Y.L. Joo, J. Mater. Sci. Lett. 22 (2003) 891-893.

30. R.S. McDonald, J. Am. Chem. Soc. 62 (1958) 1168-1178.

31. A.C. Patel, S. Li, C. Wang, W. Zhang, Y. Wei, Chem. Mater. 19 (2007) 1231-1238.

32. F. Rodríguez-Reinoso, J. Garrido, J.M. Martín-Martínez, M. Molina-Sabio, R. Torregrosa, Carbon 27 (1989) 23-32.

33. Z. Lin, M.D. Woodroof, L. Ji, Y. Liang, W. Krause, X. Zhang, J. Appl. Polymer Sci. 116 (2010) 895-901.

34. L. Ji, Z. Lin, A.J. Medford, X. Zhang, Carbon 47 (2009) 3346-3354.

35. J.F. Moulder, W.F. Stickle, P.E. Sobol, K.D. Bomben; in, Chastain, J.; King Jr., R.C. (Eds), Handbook of X-ray Photoelectron Spectroscopy, Physical Electronics, Inc., Eden Prairie, MN, 1995.

36. R.J.P. Corriu, D. Leclercq, P.H. Mutin, A. Vioux, Mater. Res. Soc. Symp. Proc. 346 (1994) 351-356.

37. G.D. Soraru, G. D'Andrea, A. Glisenti, Mat. Lett. 27 (1996) 1-5.

38. G.M. Ingo, C. Riccucci, G. Bultrini, S. Dirè, G. Chiozzini, J. Thermal Anal. Calorim. 66 (2001) 37-46.

39. S. Cavalieri, S. Subianto, L. Chevallier, D.J. Jones, J. Rozière, Chem. Commun. 47 (2011) 6834–6836.

40. N. Toshima, Macromol. Symp. 105 (1996) 111-118.

41. J.M. García-Cortés, M.J. Illán Gómez, C. Salinas Martínez de Lecea, Appl. Catal. B-Environ. 74 (2007) 313-323.

42. S.-C. Shen, S. Kawi, J. Catal. 213 (2003) 241-250.

43. P. Denton, A. Giroir-Fendler, H. Praliaud, M. Primet, J. Catal 189 (2000) 410-420.

44. S.-C. Shen, S. Kawi, Appl. Catal. B-Environ. 45 (2003) 63-76.

45. A. Bueno-López, M.J. Illán-Gómez, C. Salinas-Martínez de Lecea, Appl. Catal. A-Gen. 302 (2006) 244-249.

46. J. Dawody, M. Skoglundh, L. Olsson E. Fridell, J. Catal. 234 (2005) 206–218.

47. R. Burch, P.J. Millington, A.P. Walker, Appl. Catal. B-Environ. 4 (1994) 65-94.

48. R. Burch, J.A. Sullivan, J. Catal. 182 (1999) 489-496.

49. G.P. Ansell, A.F. Diwell, S.E. Golunski, J.W. Hayes, R.R. Rajaram, T.J. Truex, A.P. Walker, Appl. Catal. B-Environ. 2 (1993) 81-100.

50. D.K. Captain, C. Mihut, J.A. Dumesic, M. Amiridis, Catal. Lett. 83 (2002) 109-114.

51. V. Pitchon, A. Fritz, J. Catal. 186 (1999) 64-74.

52. F. Garin, P. Girard, S. Ringler, G. Maire, N. Davias, Appl. Catal. B-Environ. 20 (1999) 205-218.

53. O. Gorce, F. Baudin, C. Thomas, P. Da Costa, G. Djéga-Mariadassou, Appl. Catal. B-Environ. 54 (2004) 69-84.

54. G. Veser, F. Esch, R. Imbihl, Catal. Lett. 13 (1992) 371-382.

Figure captions

Figure 1. Coaxial electrospinning set up for the preparation of the catalysts

Figure 2. TG profiles in air atmosphere of the as-spun sub-microtubes with and without platinum and the synthetic oil used as template in the electrospinning process

Figure 3. SEM images of (a) SiT, (b) SSiT, (c) and (d) SSiT-Pt (bars length: 1 µm)

Figure 4. TEM images of (a) SSiT (bar length: 500 nm), (b) SSiT (bar length:100 nm), (c) SSiT-Pt (bar length: 200 nm) and (d) SSiT-Pt (bar length: 200 nm)

Figure 5. Platinum particle size distribution histogram of the SSiT-Pt sample

Figure 6. XRD patterns for as-spun and calcined samples

Figure 7. FTIR spectra of as-spun and calcined samples

Figure 8. Deconvoluted XPS C 1s (a) and Si 2p (b) spectra of as spun and calcined silica tubes

Figure 9. Deconvoluted XPS Pt 4f spectra of Pt-loaded samples

Figure 10. NO (400ppmv) and C_3H_6 (1500ppmv) conversion in the presence of oxygen (3%) as a function of reaction temperature, W/F_{NO}= 2.88 g·s/µmol.

Figure 11. Evolution of outlet gas concentration as a function of reaction time for SSiT-Pt catalyst a) using 200 ppm_V NO, 3%v O_2 and 1500 ppm_v C_3H_6 at 225 ºC b) 200 ppm_V NO, 3%v O_2 and 1000 ppm SO_2 at 200 ºC, c) 200 ppm_V NO, 1500 ppm_v C3H6, 3%v O_2 and 1000 ppm SO_2 at 200 ºC

Table captions

Table 1. Porous structural parameters of different silica sub-microtubes with and without platinum obtained from N_2 and CO_2 isotherms

Table 2. Atomic surface concentration (%) of different silica sub-microtubes with and without platinum determined by XPS quantitative analysis.

Figure 1

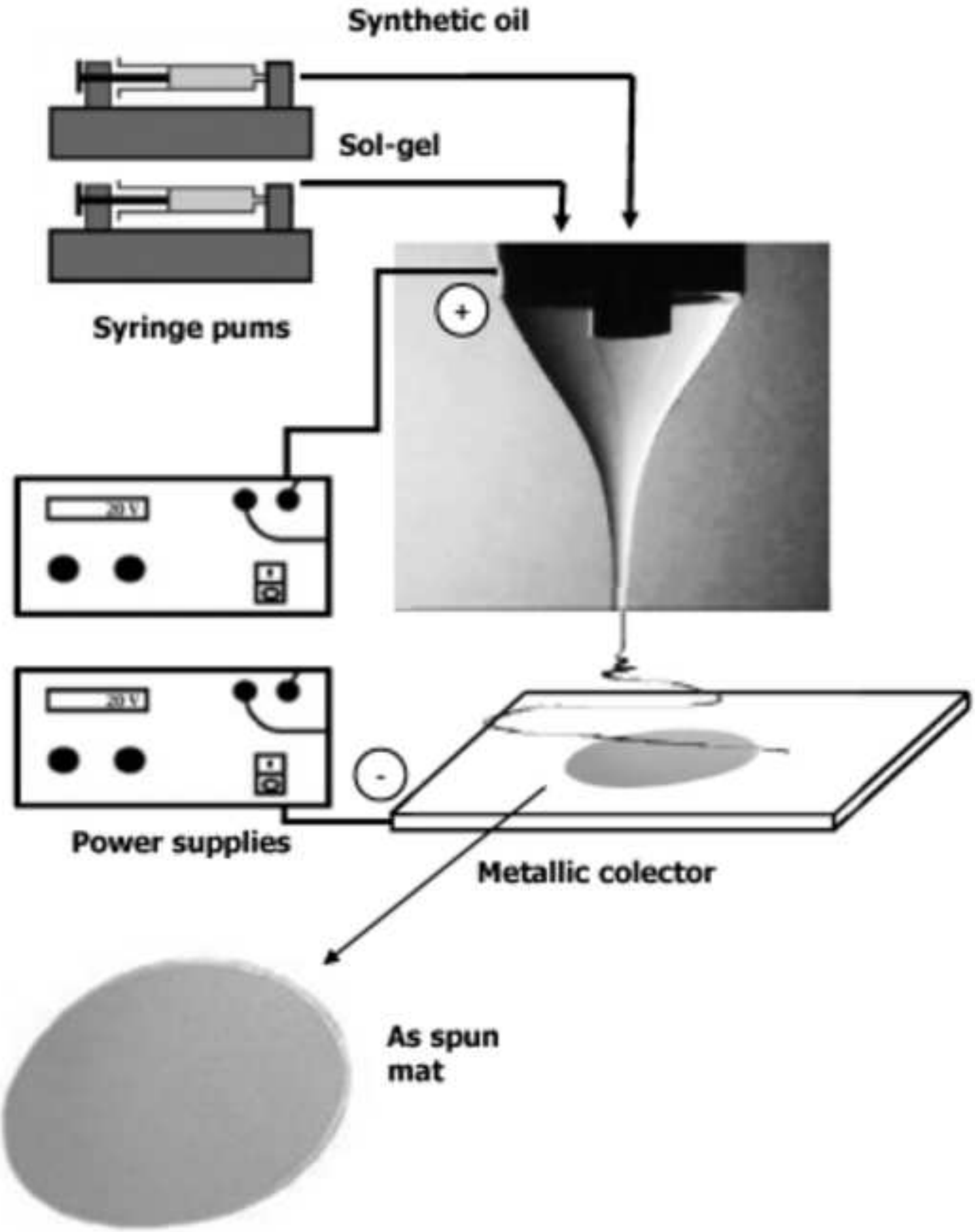
Synthetic oil
Sol-gel
Syringe pums
+
20 V
20 V
-
Power supplies
Metallic colector
As spun
mat

Figure 2

Click here to download high resolution image

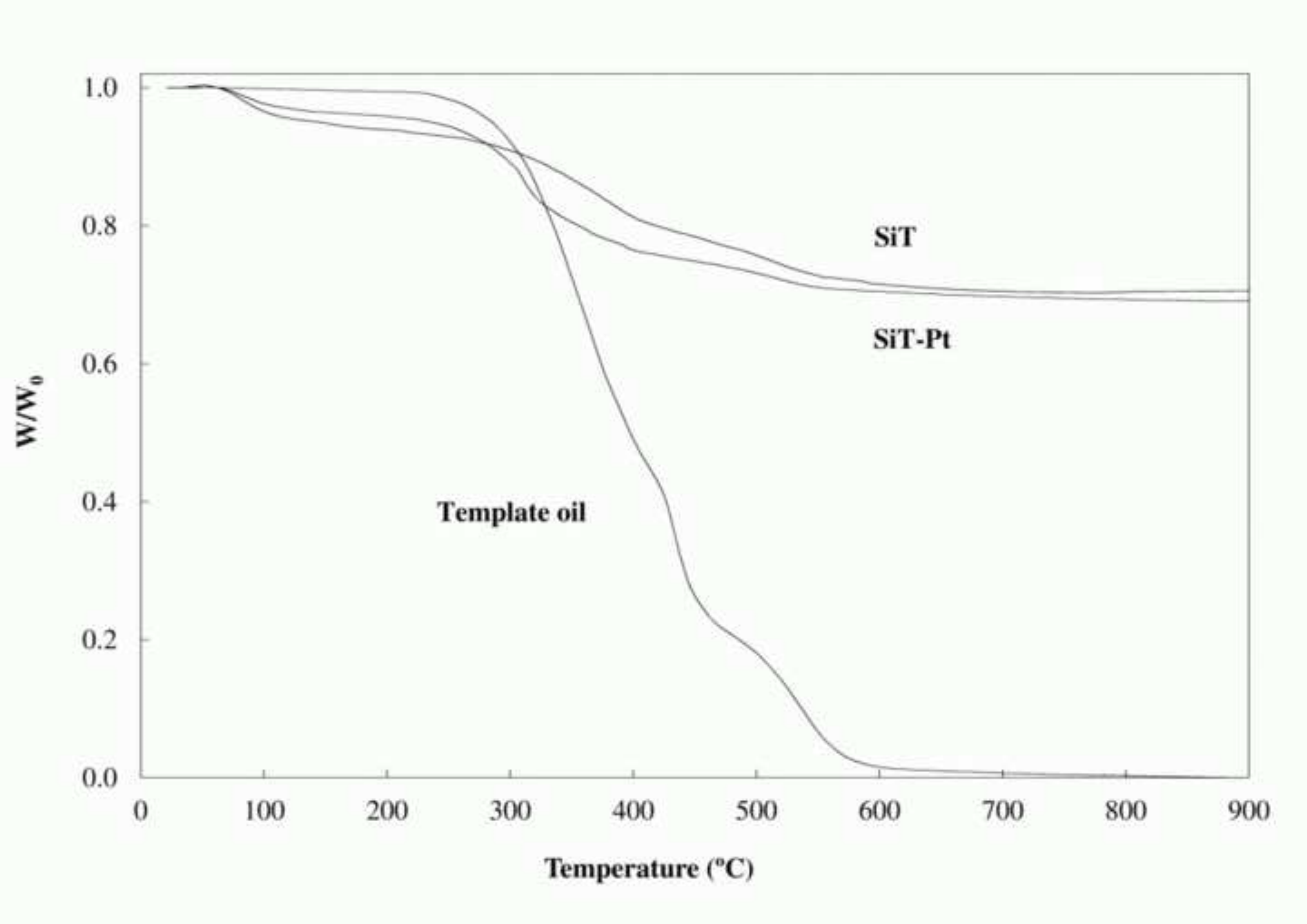

Figure 3

Click here to download high resolution image

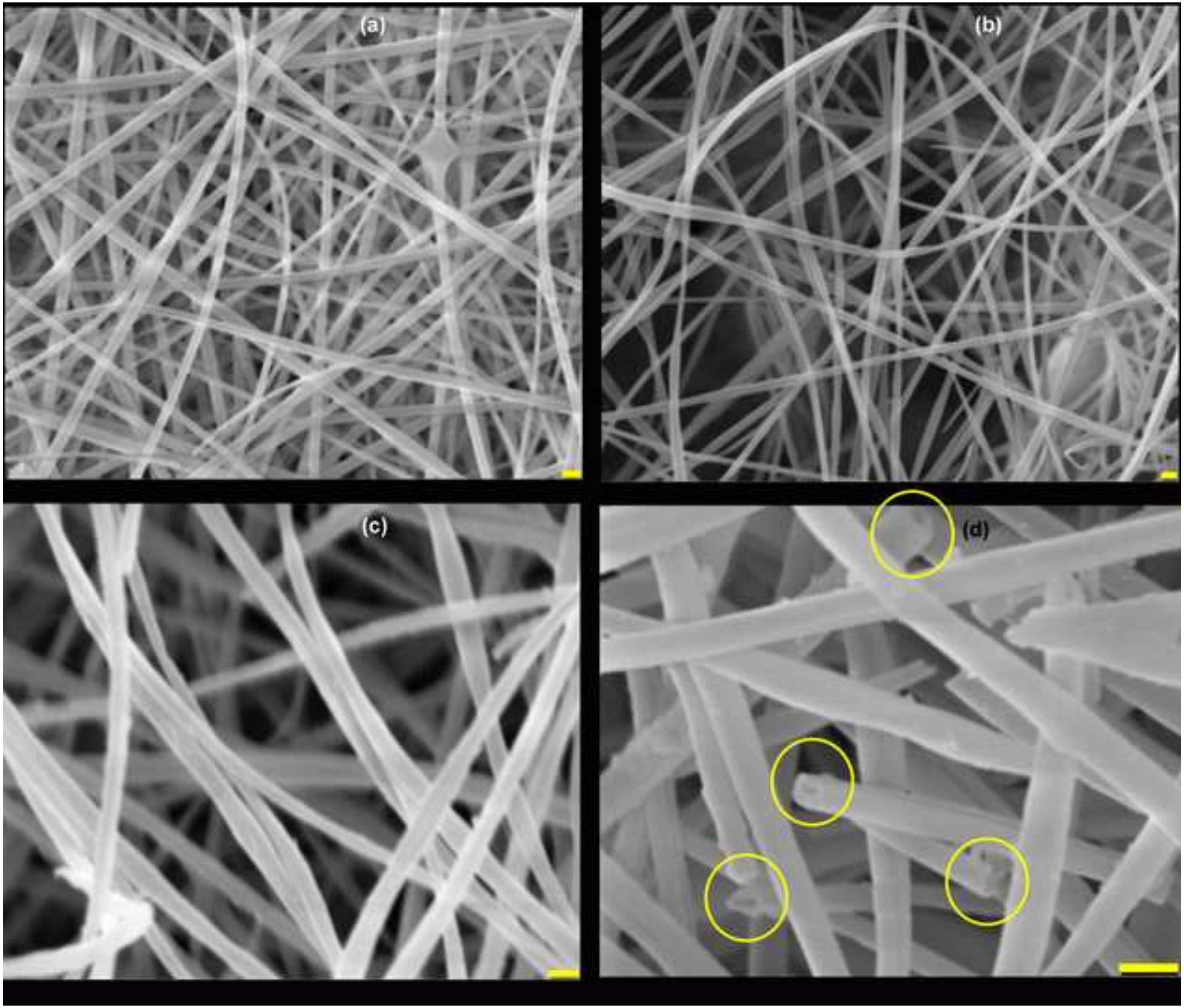

Figure 4

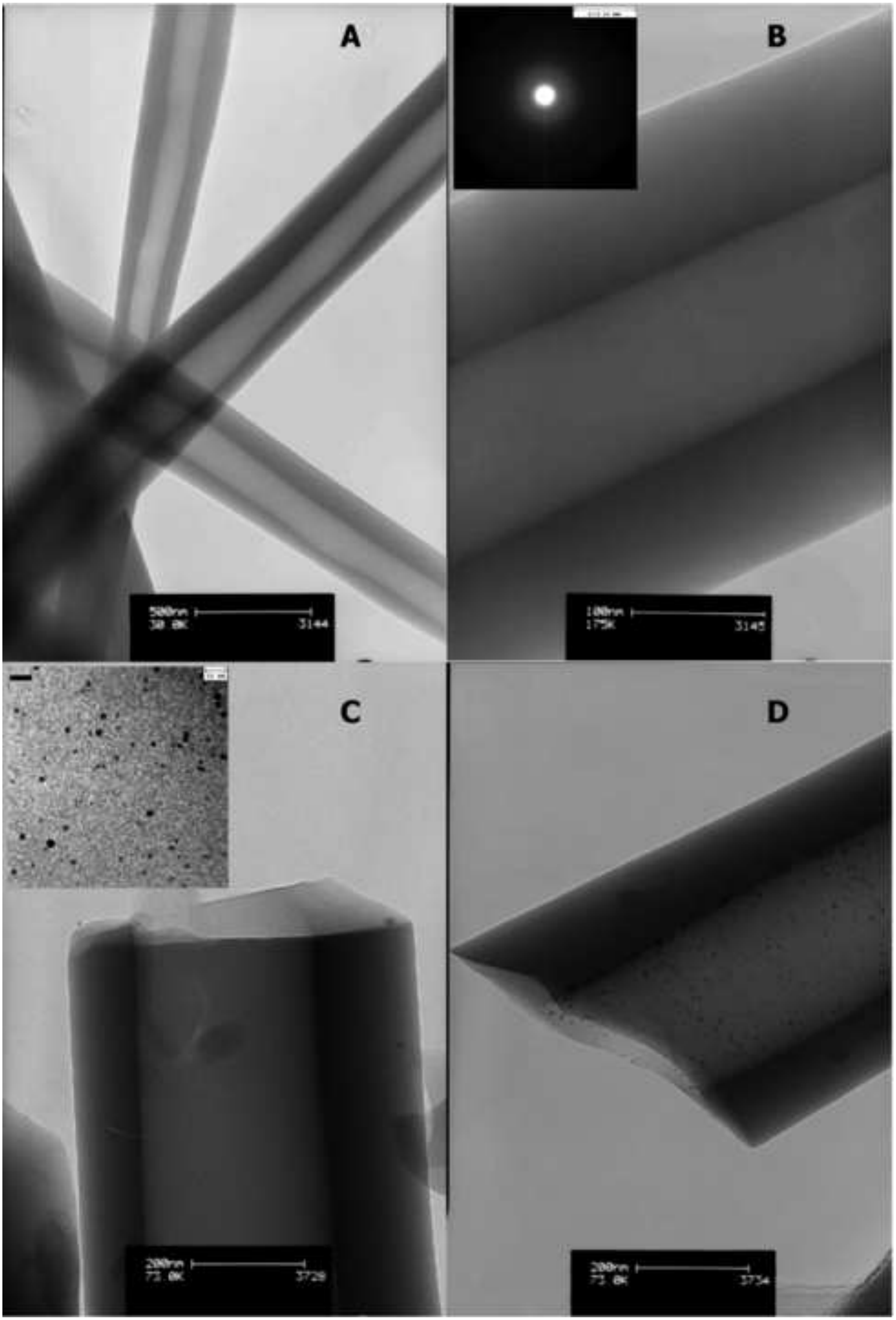
A
500nm
30.0K
3144
B
100nm
175K
3145
C
200nm
73.0K
3729
D
200nm
73.0K
3734

Figure 5

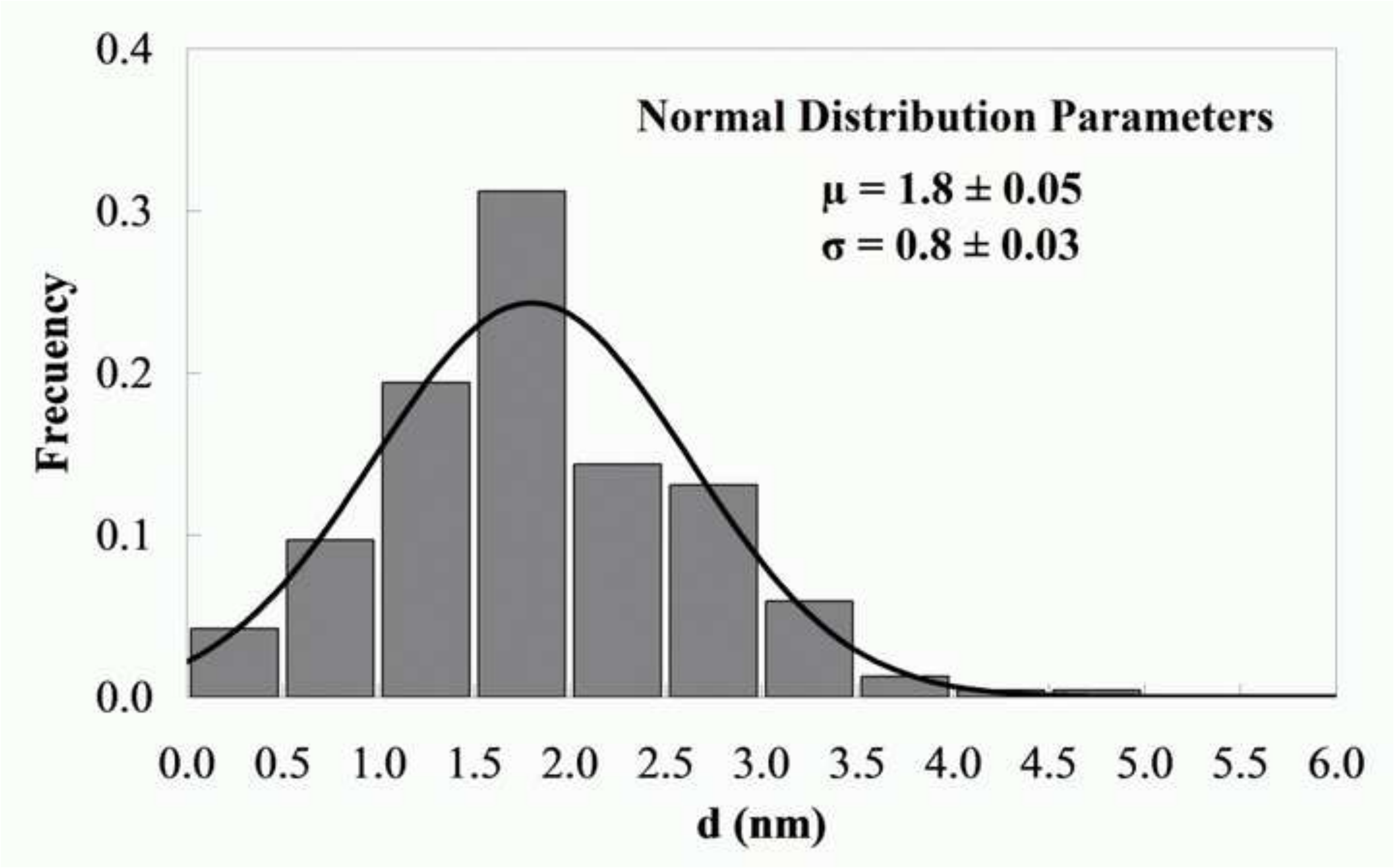
Normal Distribution Parameters
μ = 1.8 ± 0.05
σ = 0.8 ± 0.03
Frecuency
0.0
0.1
0.2
0.3
0.4
0.0
0.5
1.0
1.5
2.0
2.5
3.0
3.5
4.0
4.5
5.0
5.5
6.0
d (nm)

Figure 6

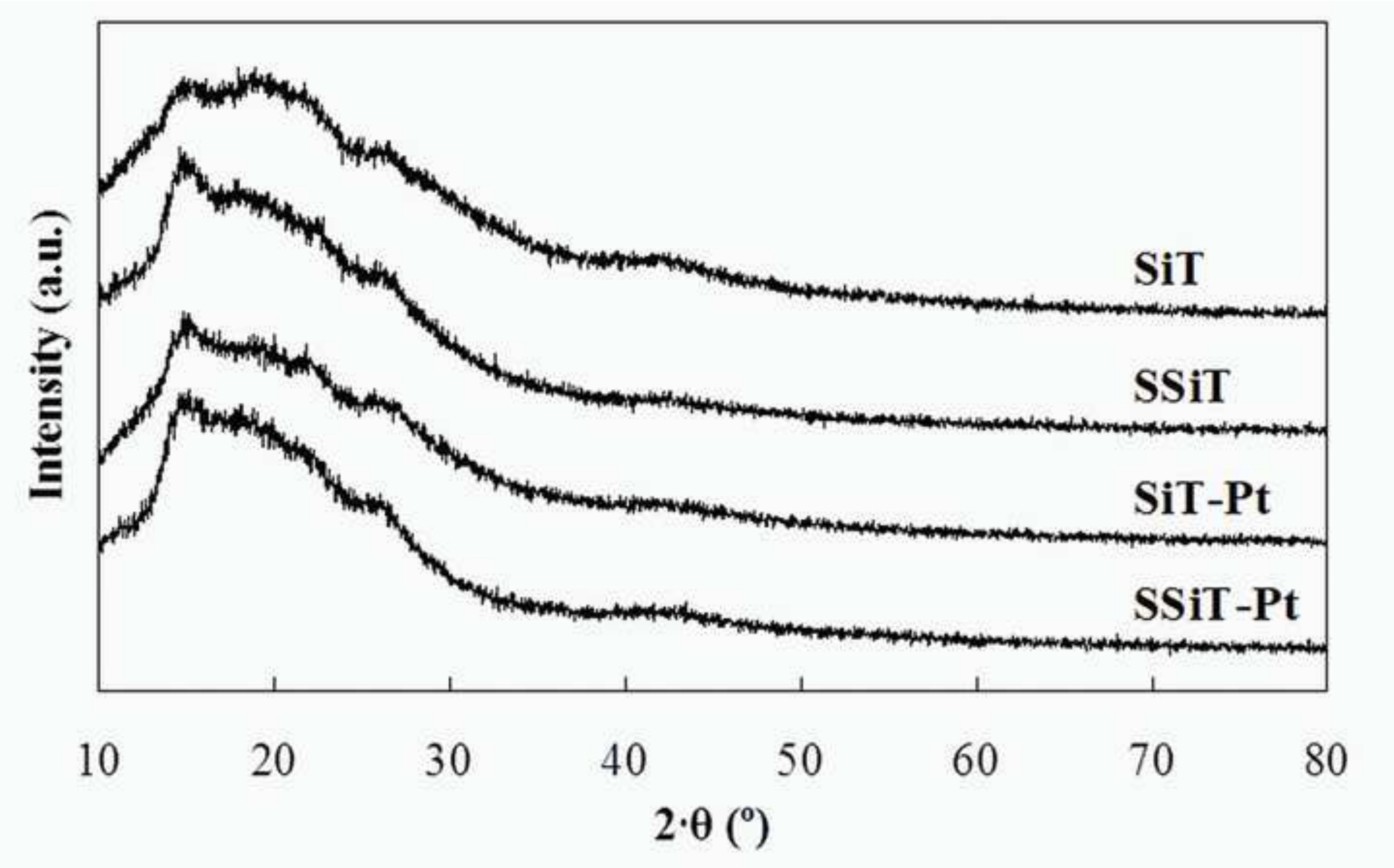

Figure 7

Click here to download high resolution image

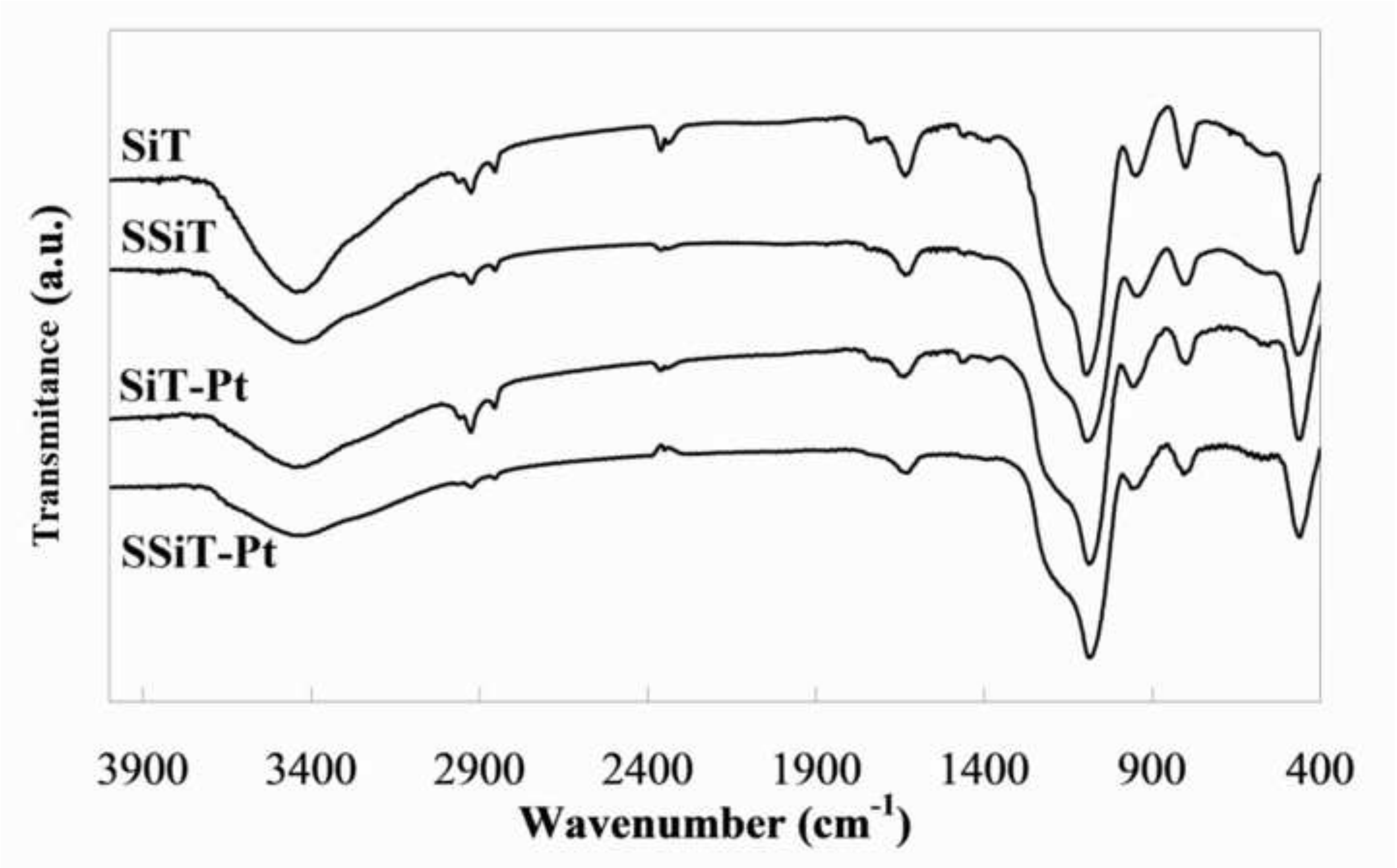

Figure 8a

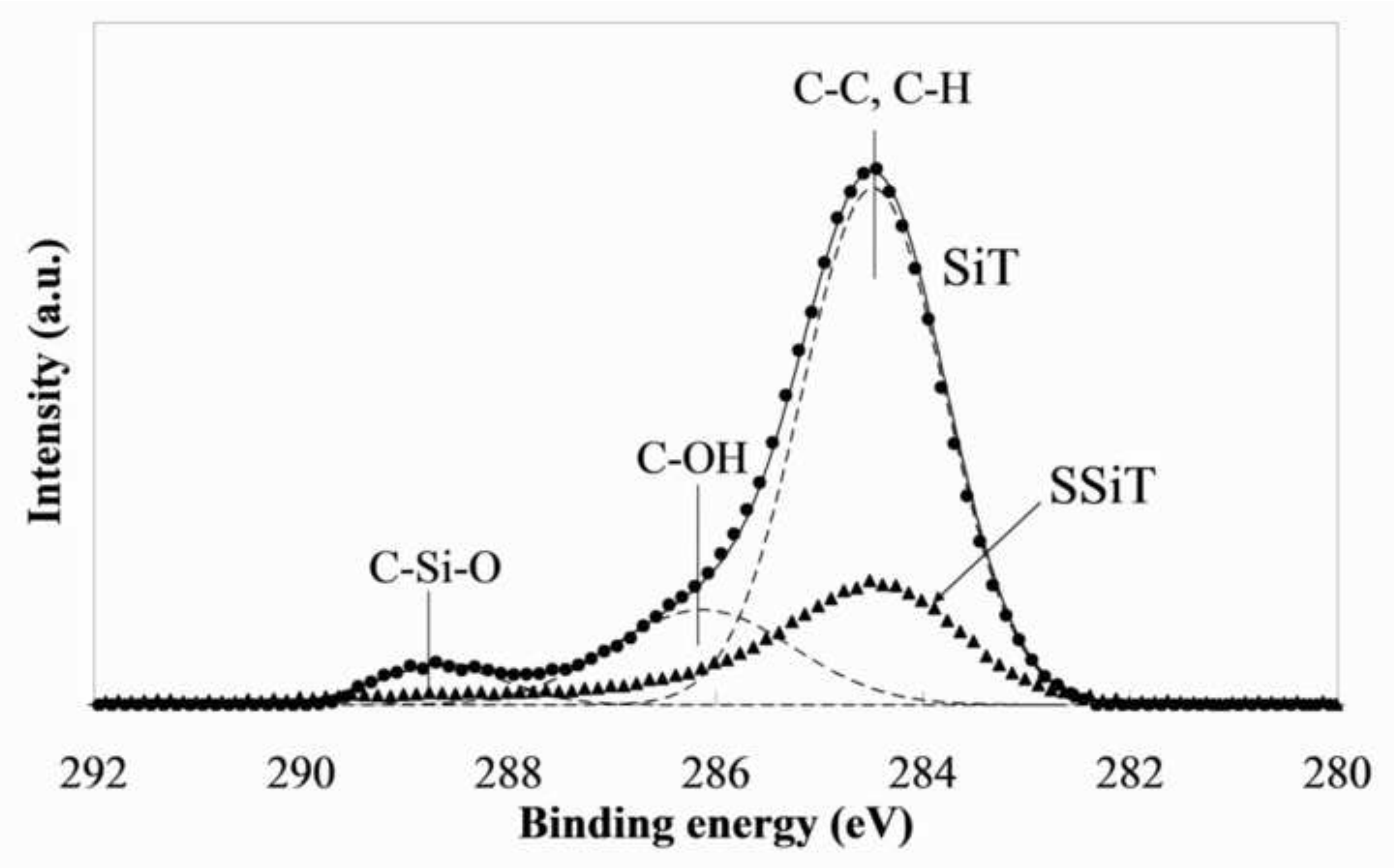
C-C, C-H
SiT
C-OH
SSiT
C-Si-O
Intensity (a.u.)
292
290
288
286
284
282
280
Binding energy (eV)

Figure 8b

Click here to download high resolution image

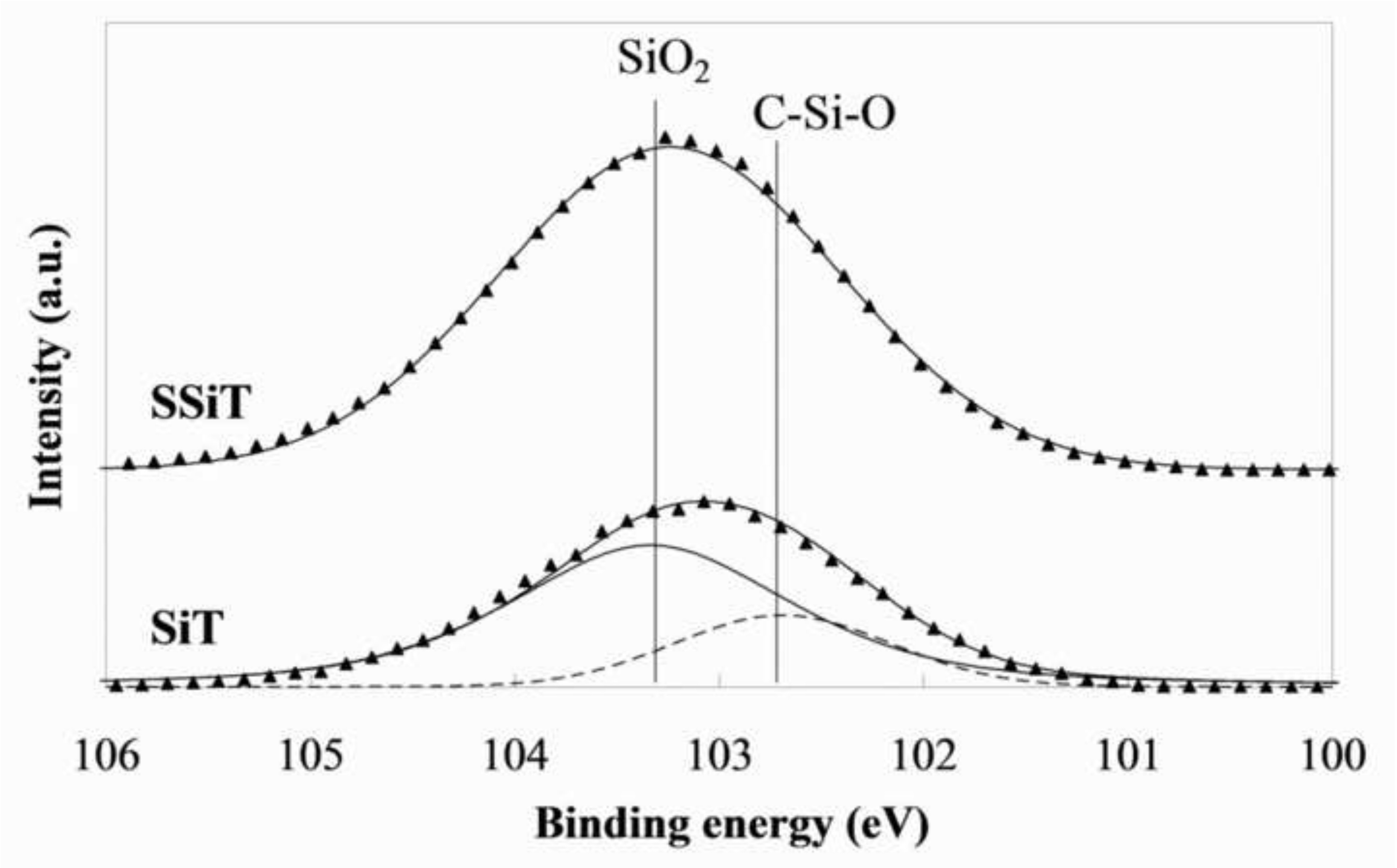

Figure 9

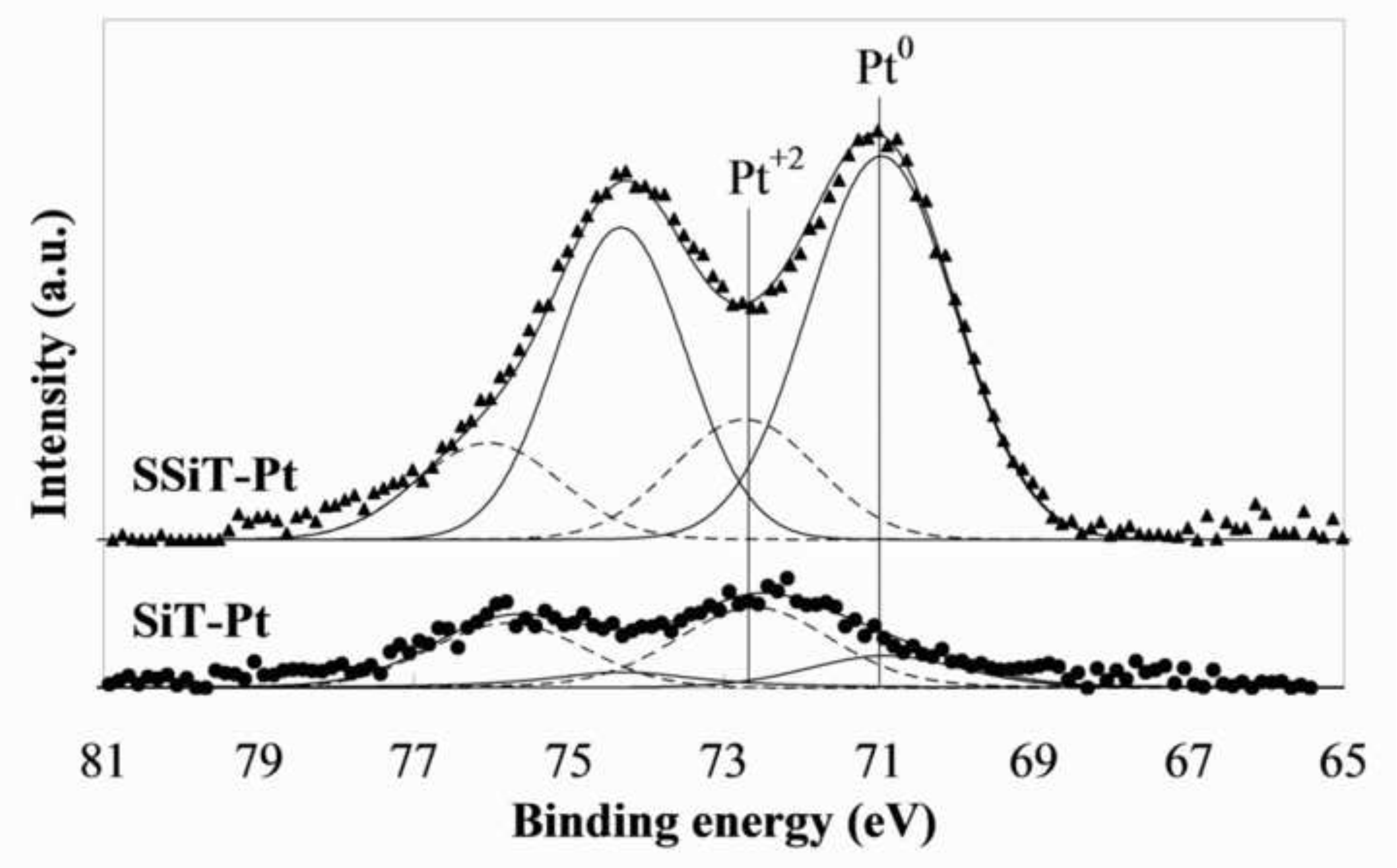
Pt^0
Pt^{+2}
SSiT-Pt
SiT-Pt
Intensity (a.u.)
81
79
77
75
73
71
69
67
65
Binding energy (eV)

Figure 10

Click here to download high resolution image

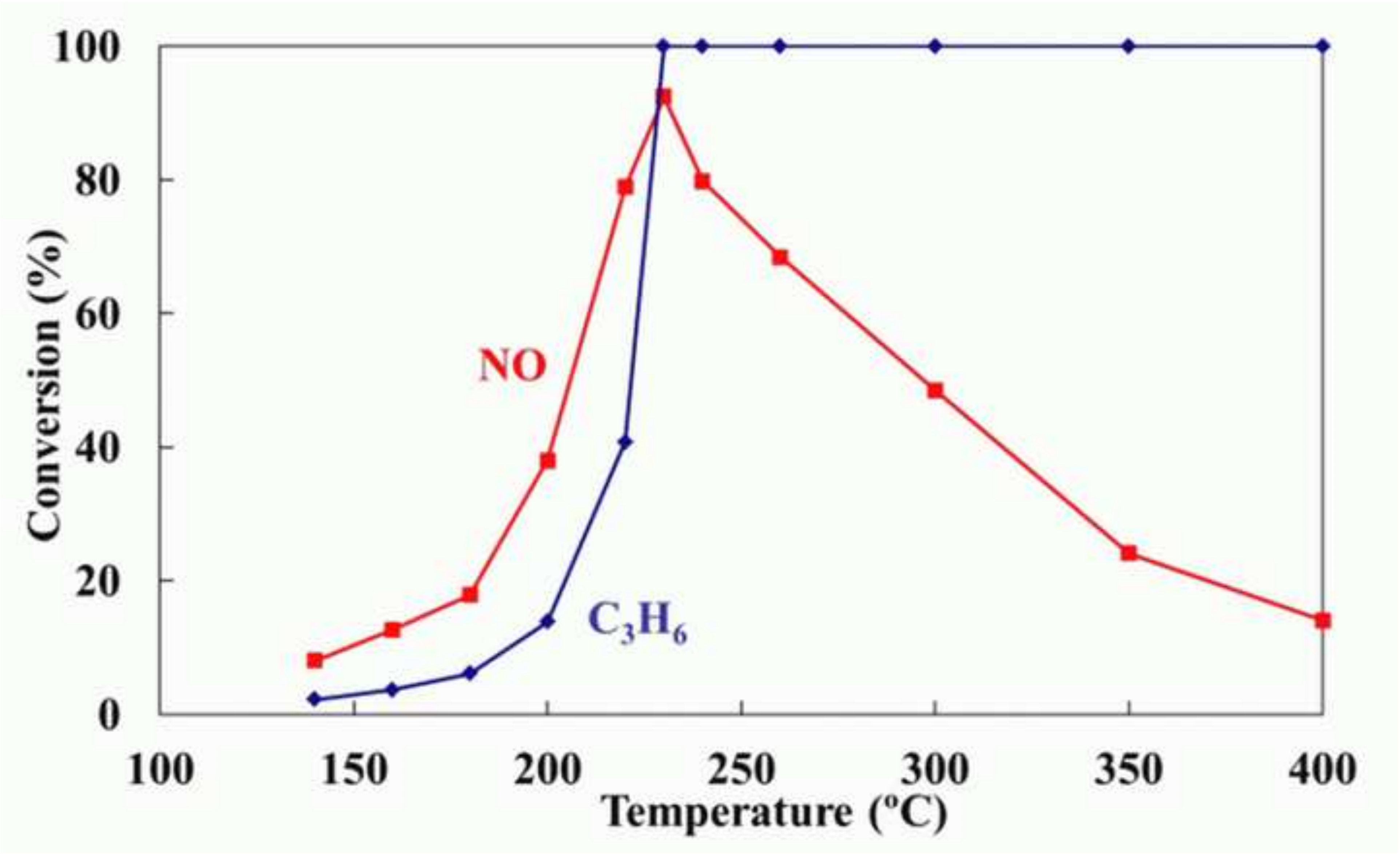

Figure 11a

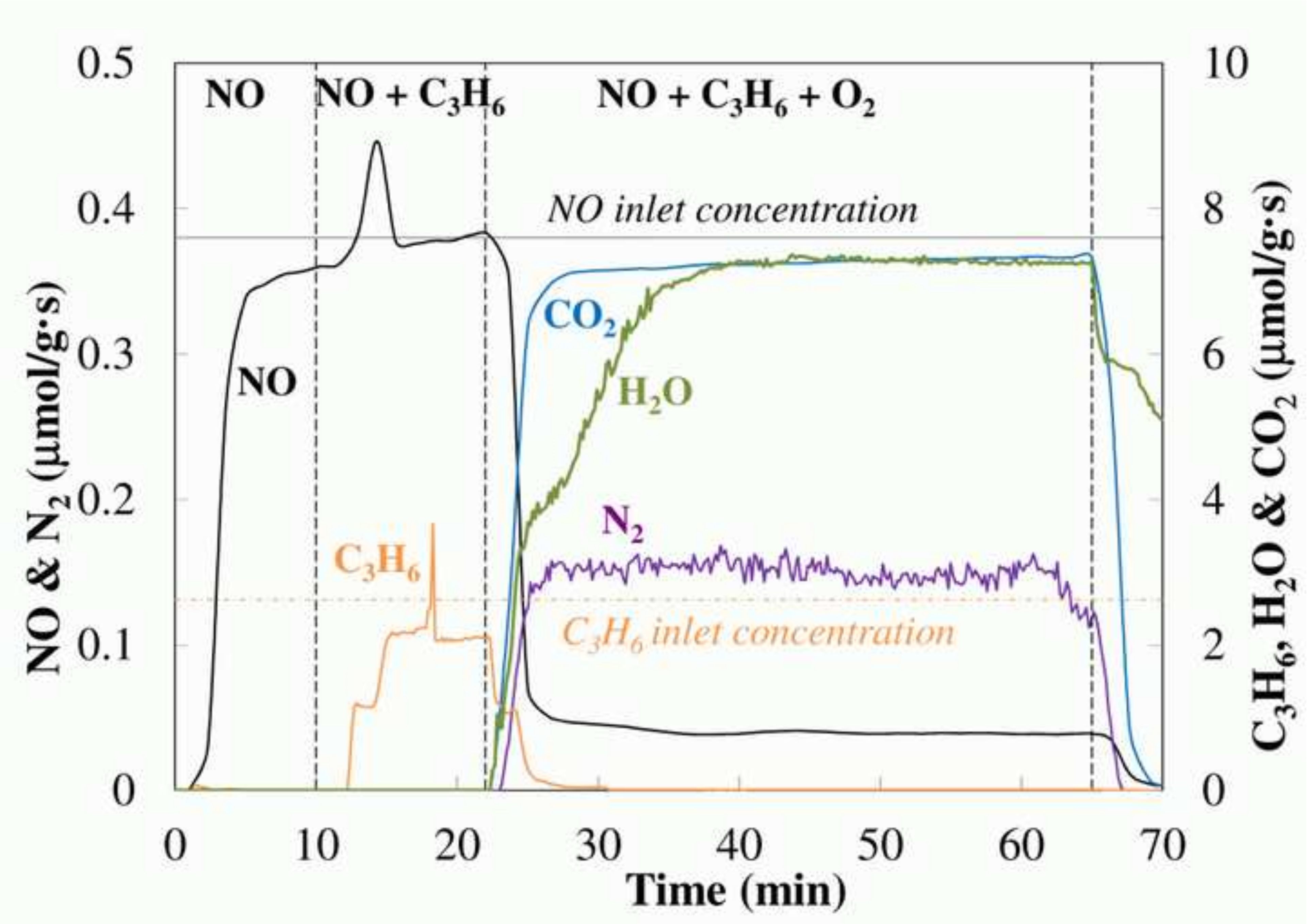
NO
NO + C_3H_6
NO + C_3H_6 + O_2
NO inlet concentration
NO
CO_2
H_2O
N_2
C_3H_6
C_3H_6 inlet concentration
NO & N_2 (μmol/g·s)
0.5
0.4
0.3
0.2
0.1
0
C_3H_6, H_2O & CO_2 (μmol/g·s)
10
8
6
4
2
0
0
10
20
30
40
50
60
70
Time (min)

Figure 11b

Click here to download high resolution image

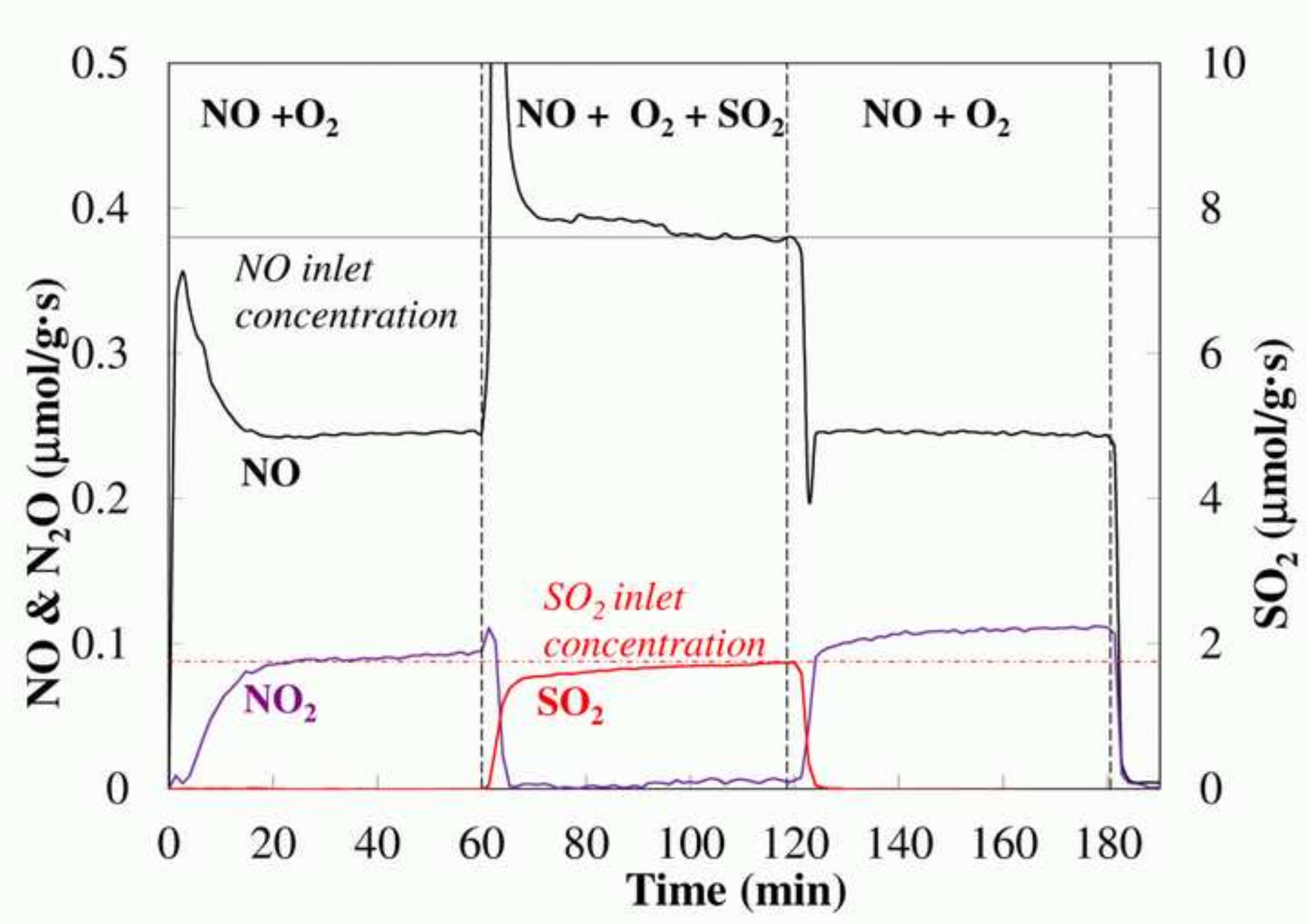

Figure 11c

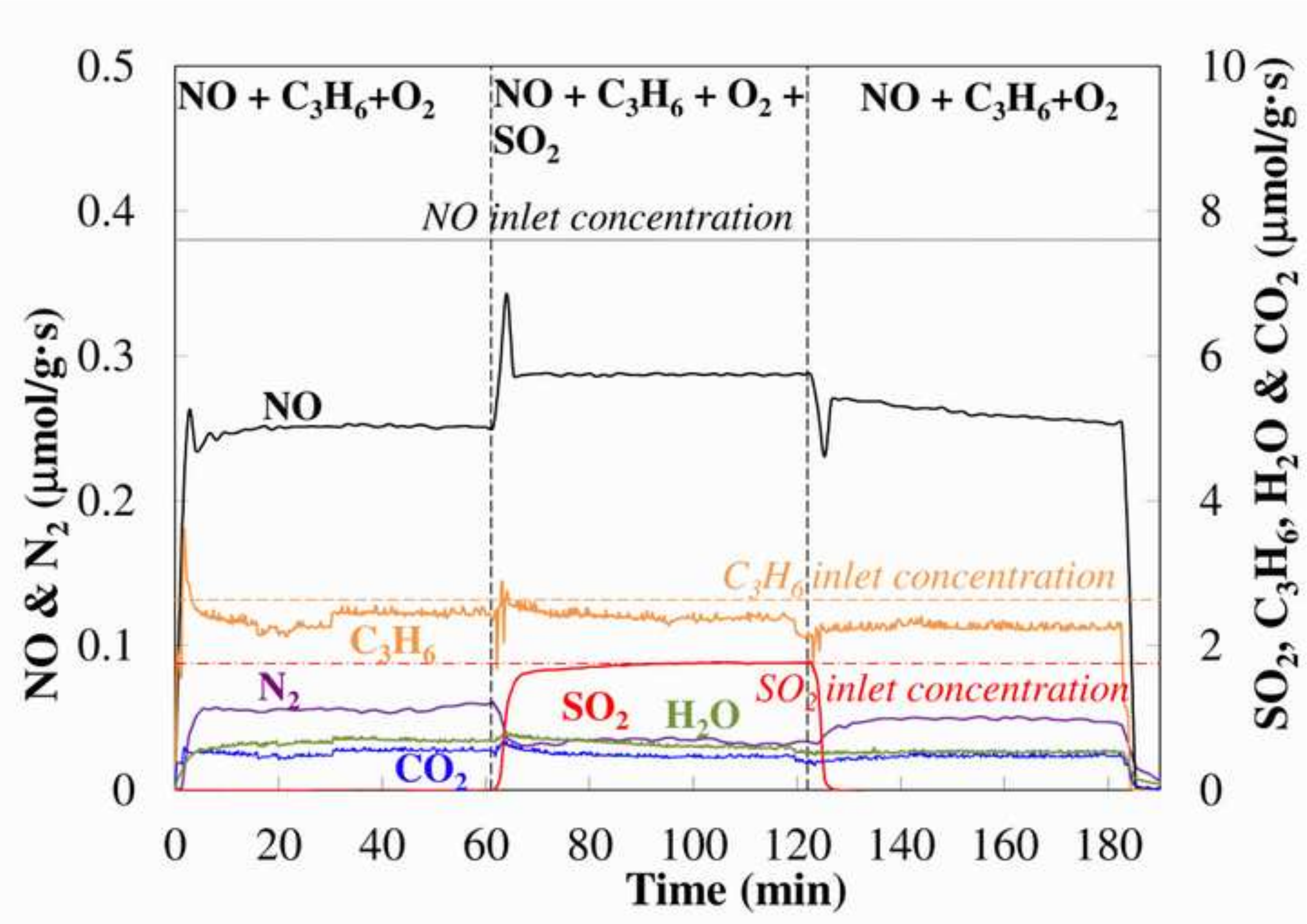
NO + C_3H_6+O_2
NO + C_3H_6 + O_2 + SO_2
NO + C_3H_6+O_2
NO inlet concentration
NO
C_3H_6 inlet concentration
C_3H_6
N_2
SO_2 inlet concentration
SO_2
H_2O
CO_2
NO & N_2 (μmol/g·s)
SO_2, C_3H_6, H_2O & CO_2 (μmol/g·s)
Time (min)
0
0.1
0.2
0.3
0.4
0.5
0
2
4
6
8
10
0
20
40
60
80
100
120
140
160
180

***Graphical Abstract (for review)**

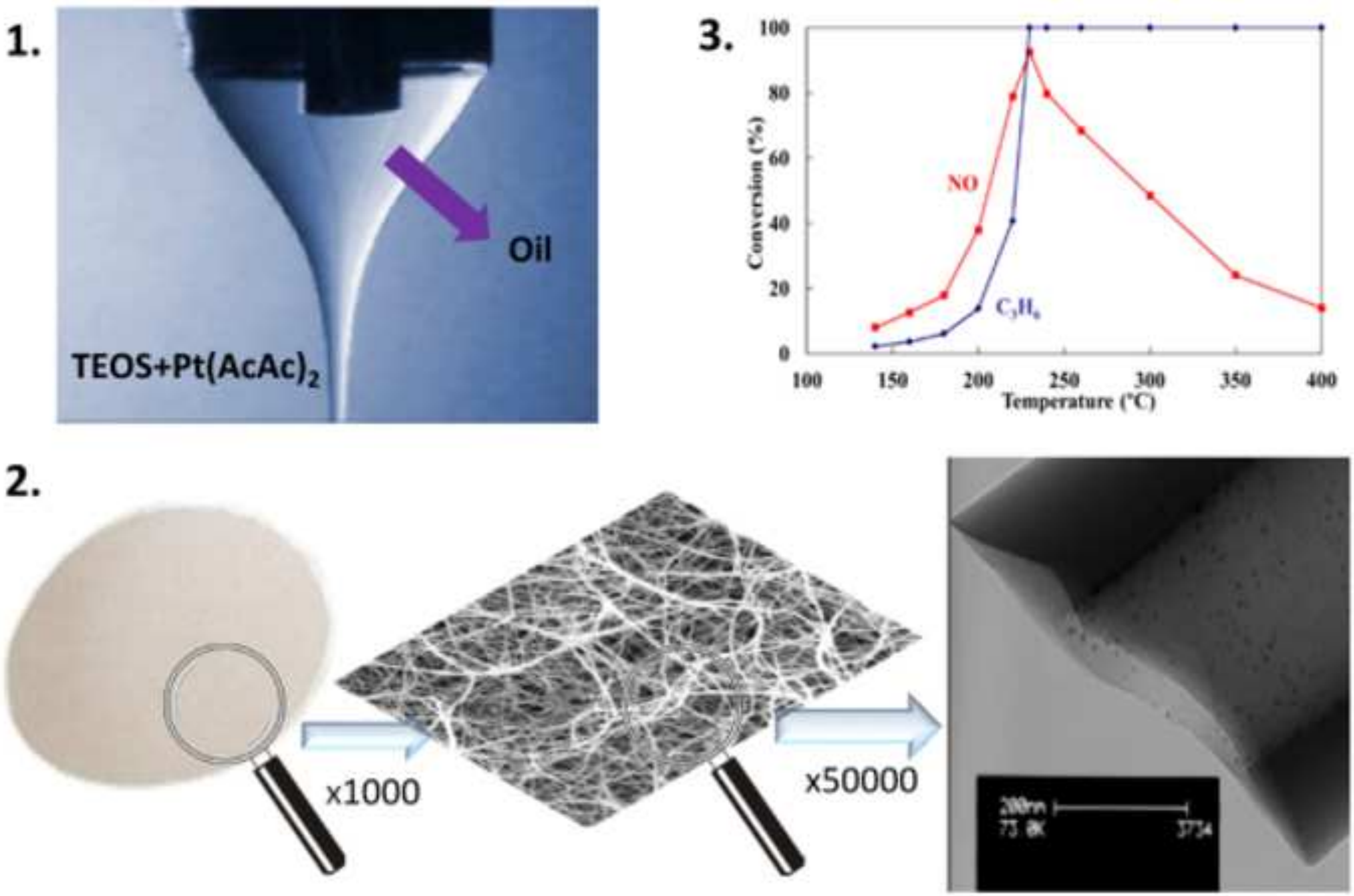

Highlights

- Mats of Pt-loaded silica nanotubes are obtained by co-axial electrospinning.
- Platinum is added within the silica precursor in one-pot procedure.
- High activity for low temperature NOx SCR with C_3H_6 in excess oxygen.
- Outstanding N_2 selectivity at the studied operation conditions.